

LONG WAVELENGTH ASTROPHYSICS

by

Liam Dean Connor

A thesis submitted in conformity with the requirements
for the degree of Doctor of Philosophy
Graduate Department of Astronomy and Astrophysics
University of Toronto

© Copyright 2016 by Liam Dean Connor

Abstract

Long Wavelength Astrophysics

Liam Dean Connor

Doctor of Philosophy

Graduate Department of Astronomy and Astrophysics

University of Toronto

2016

—

Contents

1	Introduction	1
1.1	Digital telescopes	2
1.2	The time-domain sky	4
1.2.1	Propagation effects	5
1.3	Fast Radio Bursts	9
1.3.1	Models	12
1.3.2	Empirical constraints	16
1.4	Thesis Outline	18
2	Beamforming	21
2.1	Chapter Overview	21
2.2	Introduction	21
2.3	Theory and Implementation	22
2.3.1	Geometric phase	23
2.4	Pathfinder beamformer	26
2.4.1	Instrumental phases	26
2.4.2	First coherent light	30
2.5	FRB VLBI search	34
2.5.1	Motivation	34
2.5.2	Implementation	35

2.5.3	ARO FRB search	37
2.5.4	Results	40
2.6	Conclusion	45
	Bibliography	47

List of Tables

Chapter 1

Introduction

The most interesting advances in science come not from concerted efforts to answer specific questions, but rather from exploring a new volume of parameter space. The father of observational astronomy, Galileo, did not construct Lippershey’s telescope in order to discover the Jovian satellites. Instead, he used a novel tool to investigate supra-human magnitudes and spatial resolution to observe three moons “totally invisible by their smallness” orbiting Jupiter (Drake, 1978).

The tradition has continued in the centuries since, particularly in astrophysics where we humans have little innate intuition (by definition everything we study is outside of this world). Pulsars, for example, were discovered accidentally with a radio telescope that was built to study interstellar scintillation in quasars (Hewish et al., 1968). The whole field commenced because graduate student Jocelyn Bell noticed extra “scruff” on her chart recorder. Dark matter and dark energy are two more examples of largely unpredicted, but revolutionary, discoveries (Zwicky, 1933; Riess et al., 1998; Perlmutter et al., 1999). A more recently uncovered phenomenon is the fast radio burst (FRB), a primary focus of this thesis. FRBs were discovered as a result of searching new regions of dispersion measure space at high time resolution.

1.1 Digital telescopes

A telescope’s primary purpose is to provide for us spatial, temporal, and chromatic information about electromagnetic fields on the sky. Mathematically, telescopes first perform a spatial Fourier transform (from \mathbf{x} - to \mathbf{k} -modes), traditionally with a mirror or reflector, and then another Fourier transform in time (from τ to ν) to separate the signal by wavelength, with, e.g., a diffraction grating. The electromagnetic wave’s modulus is typically then effectively squared. This destroys phase information, whether a bolometer or a charge-coupled device (CCD) is used. Modern radio telescopes carry out a similar set of steps, except at some stages they use powerful computers in place analog instrumentation. For example, channelization can be done in software rather than with diffraction. They also have the ability to preserve phase information by measuring a quantity proportional to the electric field, namely voltage.

In an era when electric fields can effectively be sampled billions of times per second, radio telescopes are becoming almost entirely digital. While the cost of constructing large single-dish telescopes is not expected to decrease substantially, the cost of building large computing clusters is, which makes it economically and strategically sensible to point one’s telescope and to channelize in software. This fact has ushered in a new era of broad-band, wide-field interferometers with large numbers of feeds. These include the Precision Array for Probing the Epoch of Reionization (PAPER), the Murchison Widefield Array (MWA), and the Low-Frequency Array (LOFAR) (Tingay et al., 2013; Parsons et al., 2014; van Haarlem et al., 2013). The Canadian Hydrogen Intensity Mapping Experiment (CHIME), which is central to this thesis, is another principally digital telescope.

Radio interferometry was first developed in the 1940s when Ryle and Vonberg constructed a dipole array at 175 MHz (Thompson et al., 1986). Based on the Michelson interferometer, it was realized that the same spatial resolution of a large dish with diameter, D , could be achieved by correlating two antennas separated by D . In a classical interferometer, the quantity we measure is called a “visibility”, denoted in this text as

$V_{m,n}$. It is the time-averaged correlation of the signals x_m and x_n .

$$V_{m,n} = \langle x_m x_n^* \rangle. \quad (1.1)$$

This can be written as an integral over all directions, $\hat{\mathbf{k}}$, on the sky, weighted by the complex gains, $g(\hat{\mathbf{k}})$, in that direction.

$$V_{m,n} = \int d^2\hat{\mathbf{k}} g_m(\hat{\mathbf{k}}) g_n^*(\hat{\mathbf{k}}) T(\hat{\mathbf{k}}) e^{2\pi i \hat{\mathbf{k}} \cdot \mathbf{d}_{m,n}} \quad (1.2)$$

Here the baseline vector between antennas m and n is given by $\mathbf{d}_{m,n}$, and $T(\hat{\mathbf{k}})$ is the sky brightness temperature in the direction $\hat{\mathbf{k}}$. This is not a thermodynamic temperature, but the temperature given by the Rayleigh-Jeans law,

$$T = \frac{c^2 I_\nu}{2\nu^2 k_b}, \quad (1.3)$$

where I_ν is specific intensity and k_b is Boltzmann's constant.

For an N -element array, there are $N(N+1)/2$ unique baselines that must be computed, i.e. for each frequency and at each time, Eq. 1.1 must be calculated $N(N+1)/2$ times. Therefore in the large- N limit, the computational cost of the correlation process is $O(N^2)$. Such a scaling means the monetary cost of large interferometers is dominated by computing hardware. One way to get around this is by choosing a highly redundant array, with antennas evenly spaced on a rectangular grid. Instead of correlating all antennas with one another, the cross-correlation theorem can be employed,

$$\mathcal{F}(\mathbf{x} \star \mathbf{x}^\dagger) = \mathcal{F}(\mathbf{x}) \mathcal{F}(\mathbf{x}^\dagger), \quad (1.4)$$

where \mathbf{x} is a vector containing signals from all N antennas. We can then calculate the cross-correlation using only spatial Fourier transforms across the array. Inverse Fourier transforming Eq. 1.4, we can reproduce Eq. 1.1 as follows,

$$\langle \mathbf{x} \star \mathbf{x}^\dagger \rangle = \mathcal{F}^{-1} \{ \mathcal{F}(\mathbf{x}) \mathcal{F}(\mathbf{x}^\dagger) \}. \quad (1.5)$$

If the antennas sit on a grid, then the transforms can be computed with Fast Fourier Transforms (FFTs), which scale as $O(N \log(N))$ instead of $O(N^2)$. This was proposed by Peterson et al. (2006) and expanded on in detail by Tegmark & Zaldarriaga (2009). CHIME has such a rectangular array configuration and will be the first large-scale FFT telescope. As we will discuss in Chapters ?? and 2, the FRB experiment will search 1024 formed beams generated by the algorithm described here.

1.2 The time-domain sky

In the early 1930s Karl Jansky built a steerable 20 MHz antenna in order to locate unaccounted-for receiver noise he had been seeing in transatlantic voice transmissions. He found the signal was periodic in sidereal day and established that the radio emission must be of astronomical origin (Jansky, 1933). In doing so he opened up a new window into the Universe. While astronomers had been observing the sky in the optical for millennia, there was now an wholly new slice of the electromagnetic spectrum with which to view the cosmos.

A similar thing could be said about the time-domain sky. Observing temporal rather than spatial fluctuations gives us access to a swath of new sources, and can help us better understand the physics of known sources. Pulsars, which proved the existence of neutron stars, could not have been discovered without time-series analysis. The first strong observational evidence for blackholes came from X-ray variations of Cygnus X-1 on timescales of days. A subset of these phenomena vary on human-timescales, but seem not to repeat. We call these transients.

Transients are ephemeral events that can last for milliseconds to months. These include gamma-ray bursts (GRBs), supernovae (SNe), and tidal disruption events. They

live in the realm of time-domain astrophysics, but are inherently hard to classify due to their fleeting nature. GRBs, for example, were discovered in the 1960s and are still not well understood. In the radio sky, known transients include flare stars, afterglows from supernovae and GRBs, solar bursts, and now FRBs.

1.2.1 Propagation effects

The two time-varying objects we discuss in this thesis are pulsars and FRBs. Since both live well outside of our solar system and both are observed at long wavelengths, one must consider the various propagation effects that occur in the intervening ionized plasma. In the following subsections we introduce the three most prominent effects. These are dispersion, Faraday rotation, and scattering.

Cold plasma dispersion

Electromagnetic waves traveling through a cold dense plasma will undergo dispersion. Here, “cold” refers to the condition that the thermal velocity of the particles in the plasma is much less than that of the wave, i.e.,

$$v_p \gg v_{ion} = \sqrt{2k_B T / m_{ion}}. \quad (1.6)$$

The dispersion results in a frequency-dependent group velocity caused by differential refractive index in an ionized plasma. The refractive index, n , is given by,

$$n = \left(1 - \frac{\omega_p^2}{\omega^2}\right)^{1/2}, \quad (1.7)$$

where ω_p is the plasma’s resonant frequency and ω is the electromagnetic wave’s frequency. The plasma frequency is

$$\omega_p = \sqrt{\frac{n_e e^2}{4\pi^2 m c}}, \quad (1.8)$$

using e , n_e , and m as the electron charge, number density, and mass respectively. Noting $n = \frac{c}{v_g}$ and plugging this plasma frequency relation into equation 1.7, we can expand about n_e . We get,

$$v_g = c \left(1 - \frac{n_e e^2 \lambda^2}{2\pi m c^2} \right). \quad (1.9)$$

This equation holds for most of the physics described in this thesis, since the dispersive electron plasmas in the IGM, ISM, and even in the remnants of supernovae are relatively diffuse, with plasma frequencies well below the bands in which we observe. For reference, typical values are $n_e^{IGM} \sim 10^{-7} \text{ cm}^{-3}$ (Madau, 2000), $n_e^{ISM} \sim 10^{-2} \text{ cm}^{-3}$ (Lyne & Graham-Smith, 1998) in our Galaxy, and in $n_e^{SNe} \sim 10^{1-3} \text{ cm}^{-3}$ in remnants (see Chapter ??).

For a single pulse, the light travel-time, t , can be written as the integral, $\int_0^D dl/v_g$, into which we can plug Eq. 1.9. The frequency-dependent time delay is then,

$$\Delta t = t - \frac{D}{c} \quad (1.10)$$

$$= 1.345 \times 10^{-3} \nu^{-2} \int_0^D n_e dl \text{ seconds.} \quad (1.11)$$

Here we have switched from angular frequency, ω , to ν in Hz. Dispersion measure (DM) can then be defined as,

$$\text{DM} \equiv \int_0^D n_e dl, \quad (1.12)$$

which is just an electron column density, and is usually reported in units pc cm^{-3} . For a telescope observing between ν_B and ν_T in GHz, the arrival-time difference between the bottom and top of the band will be,

$$\Delta t_{B,T} = 4.15 \times 10^{-3} \text{ DM } (\nu_B^{-2} - \nu_T^{-2}) \text{ seconds.} \quad (1.13)$$

While this effect delays all waves with $\nu > \nu_p$, (waves below the plasma frequency will decay exponentially and will not propagate) it is only observationally important for switch sources. Typical pulsars in our Galaxy have DMs between 10-100 pc cm⁻³, while FRB DMs can be as high as 2000 pc cm⁻³. The latter gives a dispersion delay of nearly forty seconds between 400 MHz and 800 MHz, where CHIME will observe.

Faraday rotation

If a cold plasma also has a magnetic field, a propagating electromagnetic wave's plane of polarization will be rotated. This is called the “Faraday effect” or “Faraday rotation”, named after the nineteenth century English physicist (Faraday & Martin, 1936). The rotation is caused by circular birefringence, meaning left- and right-circularly polarized light travel at slightly different speeds. Since linear polarization can be thought of as the superposition of a right- and left-handed wave, the result is a rotation of the linear polarization vector.

Like dispersion, this effect is chromatic, depending quadratically on wavelength. The linear polarization vector will be rotated by

$$\phi = 2 \text{RM} \lambda^2 \quad (1.14)$$

where RM is “rotation measure” with units rad m⁻². The extent of this rotation depends on the projection of the magnetic field onto the direction of propagation.

$$\text{RM} = \frac{e^3}{2\pi m^2 c^4} \int_0^L n_e(l) B_{\parallel}(l) dl \quad (1.15)$$

Here B_{\parallel} is the component of the magnetic field vector parallel to $d\vec{l}$. RM can be thought of as an electron-density-weighted mean value of the line-of-sight magnetic field between the observer and the source. Conventionally, it is positive for fields directed towards the observer (Manchester & Taylor, 1977).

By dividing Eq. 1.15 by Eq. 1.12 and assuming n_e is roughly constant in whatever medium the radio waves are traversing, one can estimate the average magnetic field in that direction. The ratio of RM to DM is then,

$$\frac{\text{RM}}{\text{DM}} = \frac{e^3}{2\pi m^2 c^4} \frac{\int_0^L n_e(l) B_{\parallel}(l) dl}{\int_0^L n_e(l) dl} = 0.81 \langle B_{\parallel} \rangle \mu\text{G}. \quad (1.16)$$

This is a useful tool for understanding the ISM and the structure of the Milky Way’s magnetic field.

Scattering

The least understood propagation effect in ionized astrophysical plasma is scattering. Scattered radio waves self-interfere constructively and destructively to produce intensity fluctuations (scintillation), temporal broadening, and angular broadening (Manchester & Taylor, 1977). The cause of this multi-path propagation is still greatly contested (Goldreich & Sridhar, 2006; Pen & Levin, 2014). It was assumed to be due to Kolmogorov turbulence, from which one could easily derive the frequency scalings of temporal scattering ($\tau \propto \nu^{-4}$) and angular broadening ($\theta \propto \nu^{-2}$) (Rickett, 1977). Recently, however, this picture has been called into question by pulsar scintillation observations. Stinebring et al. (2001) found parabolic arclets in Fourier-transformed “dynamic spectra” (a 2D time/frequency field) for a number of pulsars, implying that scattering occurs in just one or two screens and occurs in localized clumps. Irrespective of the underlying physics, scattering is well-studied phenomenologically. It provides a useful tool not just for studying the ISM, but also for understanding the environment of FRBs. We discuss this both in Sect. 1.3 and Chapter ??.

1.3 Fast Radio Bursts

The discovery of fast radio bursts has captivated the attention of astronomers for two reasons: their origin is a genuine mystery, the likes of which had not been seen in transient astrophysics in decades; and the problem appears to be tractable on timescales of years to a decade. There is good reason to think that with the right survey one could at least determine their radial distribution, as well as the nature of the burst source, if not specific details. This is not true of other major contemporary questions. The tensor-to-scalar ratio, r , in inflationary cosmology, or the deviation of dark energy's w from -1, could be constrained with arbitrary improvements without ever making a detection.

The first FRB was discovered in 2007 by Lorimer et al. (2007), and has since been called the “Lorimer Burst”. Its Galactic latitude ($b = -41.8^\circ$) and large dispersion measure ($DM = 375 \text{ pc cm}^{-3}$) implied that the ~ 10 millisecond burst was extragalactic (Lorimer et al., 2007). However, in the years immediately following, no fast transients were seen with DMs exceeding the expected Galactic contribution. This led to skepticism about the celestial nature of the Lorimer Burst and suspicion that it was terrestrial interference (Burke-Spolaor et al., 2011).

Suspicion that this was a one-off event was relinquished with the discovery of four more FRBs in 2010 in the High Time Resolution Universe (HTRU) survey (Thornton et al., 2013). Based on the 23 days of observing with a 0.55 deg^2 beam, they reported a surprisingly large rate of $\sim 10^4 \text{ events sky}^{-1} \text{ day}^{-1}$. Though their detection made a much stronger case for the extraterrestrial nature of FRBs, it was not unequivocally accepted. This is because until the discovery of FRB 121102 in Arecibo’s Pulsar ALFA (PALFA) survey, all FRBs had been found with the Parkes radio telescope and in its 13-beam receiver. At Parkes, an unexplained “class” of transients were found in high time resolution data that appeared to be dispersed with hundreds of pc cm^{-3} , and which lasted for ten to a few hundred milliseconds (Burke-Spolaor et al., 2011; Bagchi et al., 2012). These pulses were given the name “Perytons”, named after a mythological hybrid

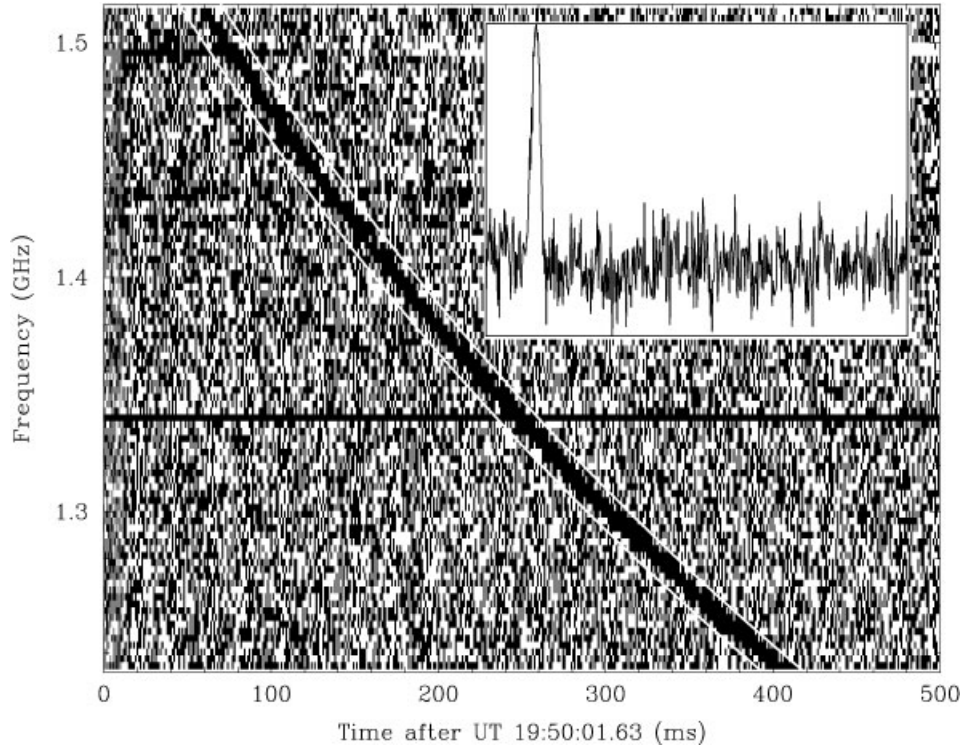


Figure 1.1: Figure reproduced from (Lorimer et al., 2007) of the so-called Lorimer Burst, which is the first known FRB.

animal.

While an astronomical origin for Perytons was excluded early on due to their multi-beam detections, it was not obvious if they were being emitted in the earth’s atmosphere naturally, or by something human-made (Katz, 2014; Dodin & Fisch, 2014; Danish Khan, 2014). It was later found by Petroff et al. (2015d) that Perytons were likely caused by an on-site microwave oven. The microwave’s magnetron was found to mimic the sweeping λ^2 dependence of truly dispersed sources when the oven’s door was opened prematurely (Petroff et al., 2015d). This made sense given the preponderance of events around local noon, i.e. lunchtime.

In the years since Thornton et al. (2013) discovered their four HTRU bursts, a dozen

or so more have been found. These are cataloged online at FRBCAT¹ (Petroff et al., 2016). As we have mentioned, Arecibo’s detection of FRB 121102 ensured that the events were not Parkes-specific. Petroff et al. (2015a) found the first FRB in real-time, as well as the first burst for which there was polarization information. FRB 110523 (Masui et al., 2015) was found in archival data from the Green Bank Telescope (GBT) intensity mapping experiment, which fortuitously saved its data with millisecond time resolution even though it was not strictly necessary for their cosmology. The completed HTRU survey also provided five new sources, found by Champion et al. (2016).

With nearly two dozen detected at the time of this writing, there is still no agreed-upon definition of an FRB. They appear to last for \sim milliseconds, have dispersion measures that are ≥ 2.5 times that of the Galactic contribution (the range has been $375 - 1600$ pc cm⁻³), and maximum flux densities of roughly a Jansky. Exceptions include the Lorimer Burst, which was ~ 30 Jy and is the brightest FRB by far, and 010621 whose DM was only about 1.4 times that expected from the Milky Way (Lorimer et al., 2007; Keane et al., 2012). At both L-band and ~ 800 MHz, a detectable rate of several thousand each day over the whole sky now seems likely (Connor et al., 2016a; Champion et al., 2016).

And such ranges are known to be incomplete. Brightness is reported as if the burst were found at the beam’s center, so each published flux is a lower limit. We also do not yet know the DM distribution. There may be a population of events with DM $\approx 10^4$ pc cm⁻³ that are either too rare to see in two dozen bursts, or to which current search algorithms have not been sensitive. Scattering is another poorly constrained parameter. FRBCAT lists five bursts with evidence for scattering, with broadening index around -4, as one would expect (Petroff et al., 2016). However, several sources have been unresolved in time, meaning their width and scattering properties are only constrained from above. The extent and prevalence of scattering is of interest for a couple reasons. One is that it

¹<http://www.astronomy.swin.edu.au/pulsar/frbcats/>

has implications for the source environment, and also because scattering is the limiting factor for low-frequency surveys, like CHIME and LOFAR (Bandura, 2014; van Leeuwen, 2014); an FRB scattered to 10 ms at 1.4 GHz would be several seconds at 400 MHz and effectively undetectable.

1.3.1 Models

Starting with the Lorimer Burst and continuing on to the four high-lat HTRU FRBs, the default assumption was that the progenitors were at cosmological distances (i.e. IGM-induced dispersion). To a lesser extent, the community seemed to assume they did not repeat, in part because of null-result follow up observations that were done (Petroff et al., 2015c), but also because bursts coming from gigaparsec distances might only have enough energy for a single event. It has been argued (Katz, 2016) that the cosmological interpretation is the most economical way of getting such large column densities of free electrons. In reality, up until recently we did not know their radial distance to better than five orders of magnitude. This is because with such a small sample of events, there was no way of knowing whether they were coming from $z \approx 0.5$, from within our Galaxy, or from our atmosphere.

A significant fraction of this thesis will focus on theoretical elements regarding fast radio bursts. Therefore it would be prudent to provide context for both the history of models that have come in and out of the picture, as well as a time-line of the observations that have informed them. We will start by enumerating the most prevalent theoretical explanations for the origin of FRBs. They will be lumped into two categories: cataclysmic, in which the progenitor is effectively destroyed, and non-cataclysmic. Note that in Chapter ?? table ?? partitions models by their distance and includes each theory's predictions for various observables.

Cataclysmic explanations

- *Blitzars:* Falcke & Rezzolla (2014) suggested that a supramassive neutron star might emit a burst of radio once it has lost its angular momentum and has begun to collapse into a black hole. This collapse will hide the star behind the event horizon and magnetic field lines will snap into place. In this model FRBs do not repeat, since the radio chirp is the object's final signal. The authors also assume these compact objects would be at cosmological distances. Given the known existence of neutron stars with mass greater than the Chandrasekhar limit, Falcke & Rezzolla (2014) conjectured that a few percent of neutron stars are supramassive and rotationally supported, and thereby eventually undergo such a transition. A natural shortcoming of this model is its lack of testable predictions. No electromagnetic counterpart is to be expected, and the proposed gravitational wave counterpart would likely be quite weak.
- *Merging compact objects:* The timescales and energies involved invoke merging compact objects. It has been suggested that NS-NS mergers similar to short-GRBs would satisfy the energetics (Totani, 2013). One might then expect a gamma-ray counterpart. Merging white dwarfs has also been proposed (Kashiyama et al., 2013). It has been suggested that the event rates may not be high enough in these models.
- *Evaporating black holes:* In this model exploding primordial black holes emit energy at wavelengths corresponding to their Schwarzschild radius, which Barrau et al. (2014) suggest. The relation,

$$\lambda_{obs} \propto (1+z) \left(\sinh^{-1} \left[\left(\frac{\Omega_{\Lambda}}{\Omega_M} \right)^{0.5} (1+z)^{-3/2} \right] \right)^{1/4}, \quad (1.17)$$

gives observable wavelengths of \sim centimeters.

Non-cataclysmic explanations

- *Galactic flare stars:* One of the first non-cosmological, non-cataclysmic models for FRBs suggested they were flaring main-sequence stars in our own Galaxy (Loeb et al., 2014). In this scenario, coronal plasma provides the DM rather than the IGM. The authors argue that the heightened energetics required by FRBs at cosmological distances theoretically motivates nearby sources. The model generically predicts repetition and, of course, overlap with known Galactic variable stars (Loeb et al., 2014; Maoz et al., 2015).
- *Magnetar flares:* Within one month of publication of the Lorimer event, Popov & Postnov (2007) had proposed that hyper-flares from cosmological magnetars could give rise to highly energetic millisecond bursts. They suggested that an extragalactic soft gamma-ray repeater (SGR) could be generated in a magnetar magnetosphere due to “tearing mode” instability. The emission mechanism of these “millisecond Extragalactic radio burst (mERBS)”, as they were - and might have ultimately been - called, was described in 2002 by Lyutikov (2002). The model requires a cosmological population to achieve the large DMs and event rates.
- *Supernova remnant pulsars:* In this model FRBs are very young pulsars, in external but non-cosmological galaxies. Their large dispersion measure from free electrons in their supernova remnants, which also Faraday rotates and scatters the burst. The dispersion measure is given by,

$$\text{DM} \approx \frac{x_e M_{\text{ej}}}{m_p \frac{4\pi}{3} v_{\text{ej}}^2 t^2} \quad (1.18)$$

, where x_e , M_{ej} are the free electron fraction and supernova ejecta mass respectively, v_{ej} , is the ejecta velocity, and t is the age. Proposed by Connor et al. (2016c) as a way of explaining all the observed phenomenology locally, it has been further

studied by Piro (2016) and Lyutikov et al. (2016). One firm prediction of this model is that the flux distribution of FRBs will be strictly Euclidean, since their progenitors are in the local Universe ($z \lesssim 0.1$). Further observational consequences of this model, including repetition, are described in ??.

- *Circum-nuclear magnetars:* This model (Pen & Connor, 2015) infers the existence of radio-loud magnetars at the centers of galaxies from the high-DM (1778 pc cm⁻³), high-RM (-6.4×10^4 rad m⁻²) SGR J1745-2900, which is < 1 pc from Sgr A*. Galactic centers would therefore provide the dispersive electron plasma and the bursts would not need to be at cosmological distances, similar to the supernova remnant model. The source of the pulse would be a radio-flare from the nuclear magnetar, similar to the mechanism in (Popov & Postnov, 2007). One issue with this model is the dearth of low-DM FRBs; since radio-loud magnetars exist outside of galactic centers, the model demands that the nuclear sources preferentially emit radio flares.
- *Super-giant pulses:* This is a class of models in which FRBs are akin to giant pulses from the Crab, but several orders of magnitude more energetic. The Crab pulsar, which exhibits the highest known brightness temperatures in the Universe, can get up to \sim MJy. Cordes & Wasserman (2016) provided a detailed investigation into the physical limitations of coherent emission around 1 GHz. Connor et al. (2016c) also use super-giant pulses as the source of the radio bursts. In that model, giant pulses are necessarily brighter earlier in the young pulsar’s life ($\lesssim 500$ years), which explains why we do not see Crab giant pulses as energetic as an extragalactic FRB. Any version of this model would expect repetition.

1.3.2 Empirical constraints

As of early 2014 no FRB observation presented any standout clues about the emission mechanism. They were all observed only in Stokes I and none had been seen to repeat. With FRB 140514, the first real-time detection, full Stokes information was recorded and immediate follow up observations were carried out in other wavelengths (Petroff et al., 2015b). It was found to have $21 \pm 7\%$ circular polarization and negligible linear polarization. No counterpart was found after 12 telescopes from radio to X-ray monitored the FRB field in the days following, ruling out local ($z < 0.3$) SNe and long GRBs (Petroff et al., 2015b).

Between late 2015 and early 2016, there was a rapid succession of significant observational claims. FRB 110523, was the first, published in fall of 2015 (Masui et al., 2015). It was the only burst after FRB 140514 for which polarimetry could be done. It was found with the GBT IM data in archival data, and had $44 \pm 3\%$ linear polarization (Masui et al., 2015). Interestingly, the source was Faraday rotated with an RM of -186 rad m^{-2} , which is roughly two orders of magnitude greater than what would be expected in the IGM (Oppermann et al., 2015). This seemed to put strain on the cosmological interpretation of FRB 110523, since the dispersion (caused by free electrons) and the Faraday rotation (caused by free electrons + a magnetic field), would be coming from two different places.

Another exceptional feature of this event was the evidence for two separate scattering screens. Scintillation was found with a $\sim \text{MHz}$ decorrelation length as well as temporal broadening at millisecond timescales. The μs scintillation is expected arise when the source enters our Galaxy, implying the ms scattering must happen somewhere local to the source (Masui et al., 2015). The FRB also showed a polarization angle swing, similar to that seen in pulsars, indicative of a rotating object. These facts, along with constraints on the dispersing electron's plasma frequencies, ruled out Galactic models. They also lent credence to rotating neutron star models, whether magnetar flares or supergiant pulses from young pulsars.

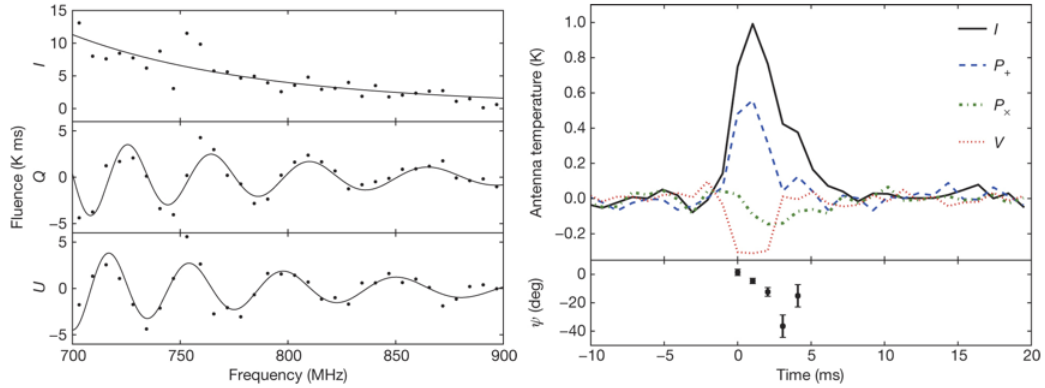


Figure 1.2: Figure adapted from Masui et al. (2015) of FRB 110523. The left panel shows the large Faraday rotation and the right panel shows the dedispersed, frequency-averaged pulse profiles for total intensity, Stokes V, and the two linear polarizations. One can also see the polarization angle swing across the burst.

Another major claim was made by Keane et al. (2016), who found a host galaxy at $z = 0.492$ that appeared to be associated with an FRB. The localization was not based on a VLBI observation, but rather a coincident radio “afterglow” in the same $\sim 13''$ Parkes field. Part of a multi-wavelength follow up, the Australia Telescope Compact Array (ATCA), observing at 5.5 and 7.5 GHz, found a radio source whose flux seemed to fall off a factor of a few in roughly 6 days. The authors interpreted this as a fading transient, not unlike radio afterglows of short GRBs, favouring the compact object merger scenario. However, the validity of this galaxy’s association with the FRB has been called into question. Shortly after the press release of (Keane et al., 2016), Williams & Berger (2016) did a further observation suggesting the source was in fact a *variable* rather than a transient, the latter of which are quite rare.

By far the most important new observation in the field is the discovery of FRB 121102’s repetition (Spitler et al., 2016). 121102 was found to repeat 10 times in (Spitler et al., 2016) and 6 additional times in (Scholz et al., 2016). With one fell swoop the numerous models in the cataclysmic class were falsified. The exception being if there are two or more populations of FRBs with disparate progenitors, in which case “Type A FRBs”, for instance, are known to be non-destructive. The sub-bursts were all also detected with Arecibo, many of them getting down to the telescope’s fluence limit, implying most of its bursts were undetectable (Spitler et al., 2016; Scholz et al., 2016). Its DM changed by less than measurement uncertainty of $\sim 6 \text{ pc cm}^{-3}$ over the course of several years, though the spectral properties varied wildly from burst to burst. Finally, its repetition was highly non-Poissonian, with 6 of the first 10 appearing in single twenty minute pointing, despite monitoring the field for over ten hours. Such non-Poissonian behaviour was predicted in (Connor et al., 2016b) and has consequences for survey strategy.

1.4 Thesis Outline

In Chapter ?? we introduce the Canadian Hydrogen Intensity Mapping Experiment (CHIME). We start by describing the science goals of the telescope’s three back-ends: cosmology, pulsar, and FRB. The instrument is discussed, including a step-by-step outline of the signal chain. This chapter’s purpose is to provide context for the other chapters, which either involve CHIME directly or are relevant to its science. Also presented is early analysis work that I have done, including the discovery of various unexpected beam properties of the CHIME Pathfinder. A simple simulation of aliasing with a 128-feed cylinder is described, which I built. However, since this is a large collaboration, most of the work in this chapter was done by other members of CHIME. For example, the F-engine was built by Kevin Bandura, Jean Francois Trempe, and Matt Dobbs, but it still seemed necessary to describe that step in the data processing. Richard Shaw, Ue-Li Pen,

and Kris Sigurdson developed the “m-mode” formalism and pipeline, but it is essential to the science of CHIME cosmology. Details about the instrument in this chapter overlap with the work published in (Bandura, 2014), (Newburgh et al., 2014), and (Berger et al., 2016), all of which I co-authored.

In Chapter 2 we delineate the commissioning of CHIME Pathfinder’s beamformer, prefaced by a mathematical introduction to digital beamforming. The work described was done largely by myself, but with the aid of several key people. Andre Recnik was instrumental in networking and miscellaneous computing issues related to the back-end. My supervisor, Keith Vanderlinde was critical in guiding this project in the right direction. The real-time FRB VLBI survey, starting with the burst-search that was attached to the Pathfinder’s formed-beam, relied on the direction of Ue-Li Pen and the programming of Kendrick Smith and Kiyo Masui. Kendrick wrote a mutli-threaded real-time VDIF packet assembler, and Kiyo wrote a tree-dedispersion burst search in **Python**.

Chapter ?? presents a theory for the origin of FRBs in which the bursts are from extragalactic but non-cosmological pulsars in the remnants of recent supernovae. We published this model in Monthly Notices of the Royal Astronomical Society (MNRAS) at a time when FRBs were not known to repeat and most authors assumed they were cosmological and cataclysmic (Connor et al., 2016c). This work was done in collaboration with Ue-Li Pen and Jonathan Sievers. It was Jonathan Sievers’ idea to place FRBs in young, compact SNe remnants. I then built a model to represent that environment, infer its consequence, and feasibility in terms of event rate and energetics. With Ue-Li I also worked on the observables of the supernova remnant hypothesis as well as other models. These are included in table ??.

Chapter ?? is called “FRB Statistics”. In it we analyze a number of statistical problems that have come up since the discovery of FRBs. These include their purportedly non-uniform latitudinal distribution and constraints on their repeat rate. These sections were adapted from a paper published in MNRAS in collaboration with Ue-Li Pen and

Niels Oppermann (Connor et al., 2016b). My contribution to this paper included building a model for FRB repetition based on $1/f$ noise and doing mock-follow-up Monte Carlo simulations. Working with Ue-Li, I also developed a test for the latitudinal dependence of the burst-rate that is based on a biased coin flip. This chapter later investigates the all-sky event rate below L-band, and forecasts for CHIME FRB and several other low-frequency experiments. The corresponding sections were derived from (Connor et al., 2016a), again published in MNRAS. As lead author I carried out most of the calculations, excluding the frequentist/Bayesian estimates for event rate, which were conceived of by Niels Oppermann. Hsiu-Hsien Lin and Kiyo Masui, who are members of the GBT IM experiment, provided details about the survey and its dataset. Ue-Li Pen was crucial in the overall direction of the research, particularly in focusing on easily calculable statistics and the idea to forecast by comparing similar surveys. The final paper whose work ended up in Chapter ?? was (Oppermann et al., 2016), accepted to MNRAS. This work was regarding the signal-to-noise distribution of FRBs and the use of a V/V_{\max} test. Niels Oppermann created the plots and wrote code to calculate the α /event-rate posterior, but most of the theoretical work was done in meetings with Ue-Li Pen, myself, and Niels.

The final chapter investigates the sub-millisecond structure of individual pulses from B0329+54. The “microstructure” is studied in full polarization, and its quasi-periodicities are found to be common within a pulse for all Stokes parameters, but not common between pulses. This work was done with the supervision of Ue-Li Pen, who provided physical insight and guidance on the project’s direction.

Chapter 2

Beamforming

2.1 Chapter Overview

This chapter outlines the basic theory behind digital beamforming, and describes the commissioning of the first beamformer on CHIME Pathfinder. This includes the synthesis of several different software packages, the implementation of a scheduler, and an automated point-source calibration daemon that removes drifting instrumental gains in real-time. We will also detail early pulsar work and the beamformer’s first light. This includes the first ever coherent pulsar observations taken with CHIME. Finally, the creation of an ongoing VLBI FRB search between the DRAO and ARO will be outlined, starting with a real-time 24/7 transient search on the Pathfinder’s synthetic beam. We discuss early results, including the false-positive rate and distribution, as well as the implications of a non-detection on the FRB brightness distribution, $N(S)$. We exclude $\alpha < 0.6$ with 95% confidence, which provides a new lower-bound on that parameter.

2.2 Introduction

Beamforming is a signal processing technique that allows for spatial filtering, and has greatly benefited a diverse set of fields from radar and wireless communications to radio

astronomy (van Veen & Buckley, 1988). Whether being used in phased-array RADAR (Zrnic et al., 2007), ultrasonic imaging (Macovski, 1983), or wide-band radio astronomy (Tingay et al., 2013), beamforming allows for heightened sensitivity or output to select spatial modes. This usually involves a sensor (in our case an antenna) being used alongside a processor (in our case, a computing cluster) (van Veen & Buckley, 1988). Modern astronomy will benefit greatly from this technology, and beamforming is particularly essential to CHIME. The pulsar back-end will rely on brute-force beamforming in order to track ten sources at a time, 24/7. The FRB experiment will FFT-beamform to generate 1024 fan-beams, in order to search them in real time for radio transients. Finally, the cosmology experiment has always left itself the option of beamforming, whose computing cost scales as $N \log N$, as an alternative to the full- N^2 correlation.

2.3 Theory and Implementation

By coherently combining the voltages of a multi-element array, sensitivity can be allocated to small regions of the sky and the array’s effective forward gain can be increased. The signal from each antenna, x_n , is multiplied by a complex weight whose phases, ϕ_n , are chosen a priori to maximally destructively interfere radio waves in all directions but the desired pointing. After applying such weights, the signals from all antennas are combined to give the formed beam voltage stream, X_{BF} .

$$X_{\text{BF}} = \sum_{n=1}^N a_n e^{i\phi_n} x_n \quad (2.1)$$

Here a_n are real numbers that can be used as amplitude weightings for the antennas. If we define a more general complex weighting, $w_n \equiv a_n e^{i\phi_n}$, and switch to vector notation, Eq. 2.1 becomes,

$$X_{\text{BF}} = \mathbf{w} \mathbf{x}^T. \quad (2.2)$$

In general, X_{BF} and \mathbf{x}^T will be functions of time and frequency. This is also true for \mathbf{w} , unless one needs a static, non-tracking beam – which is the case for the CHIME Pathfinder’s transient search, described in Sect. 2.5. We can write this explicitly as follows,

$$\mathbf{w}_{t\nu} = (a_1(\nu)e^{i\phi_1(\nu)}, a_2(\nu)e^{i\phi_2(\nu)}, \dots, a_N(\nu)e^{i\phi_N(\nu)}) \quad (2.3)$$

$$\mathbf{x}_{t\nu} = (x_1(t, \nu), x_2(t, \nu), \dots, x_N(t, \nu)). \quad (2.4)$$

The voltage stream, X_{BF} , is then effectively squared and integrated to give a visibility stream. In the case of CHIME, X_{BF} corresponds to a single polarization so to get the full Stokes information one must compute the north-south polarization’s autocorrelation, the east-west autocorrelation, and their cross-correlation. The Stokes vector can be written as,

$$\mathbf{S} = \begin{pmatrix} I \\ Q \\ U \\ V \end{pmatrix} = \begin{pmatrix} X_{\text{ew}}X_{\text{ew}}^* + X_{\text{ns}}X_{\text{ns}}^* \\ X_{\text{ew}}X_{\text{ew}}^* - X_{\text{ns}}X_{\text{ns}}^* \\ \Re(X_{\text{ew}}X_{\text{ns}}^*) \\ \Im(X_{\text{ew}}X_{\text{ns}}^*) \end{pmatrix}. \quad (2.5)$$

2.3.1 Geometric phase

We now need to calculate ϕ_n across the array. Ignoring instrumental phases for now, one can compute the geometric phases for an antenna by projecting its position vector, \mathbf{d}_n , onto the pointing vector, $\hat{\mathbf{k}}$. This gives,

$$\phi_n = \frac{2\pi}{\lambda} \mathbf{d}_n \cdot \hat{\mathbf{k}}, \quad (2.6)$$

where we have taken \mathbf{d}_n to be the baseline vector between feed n and an arbitrary

reference point and ϕ is the corresponding phase difference. A sketch for this is shown

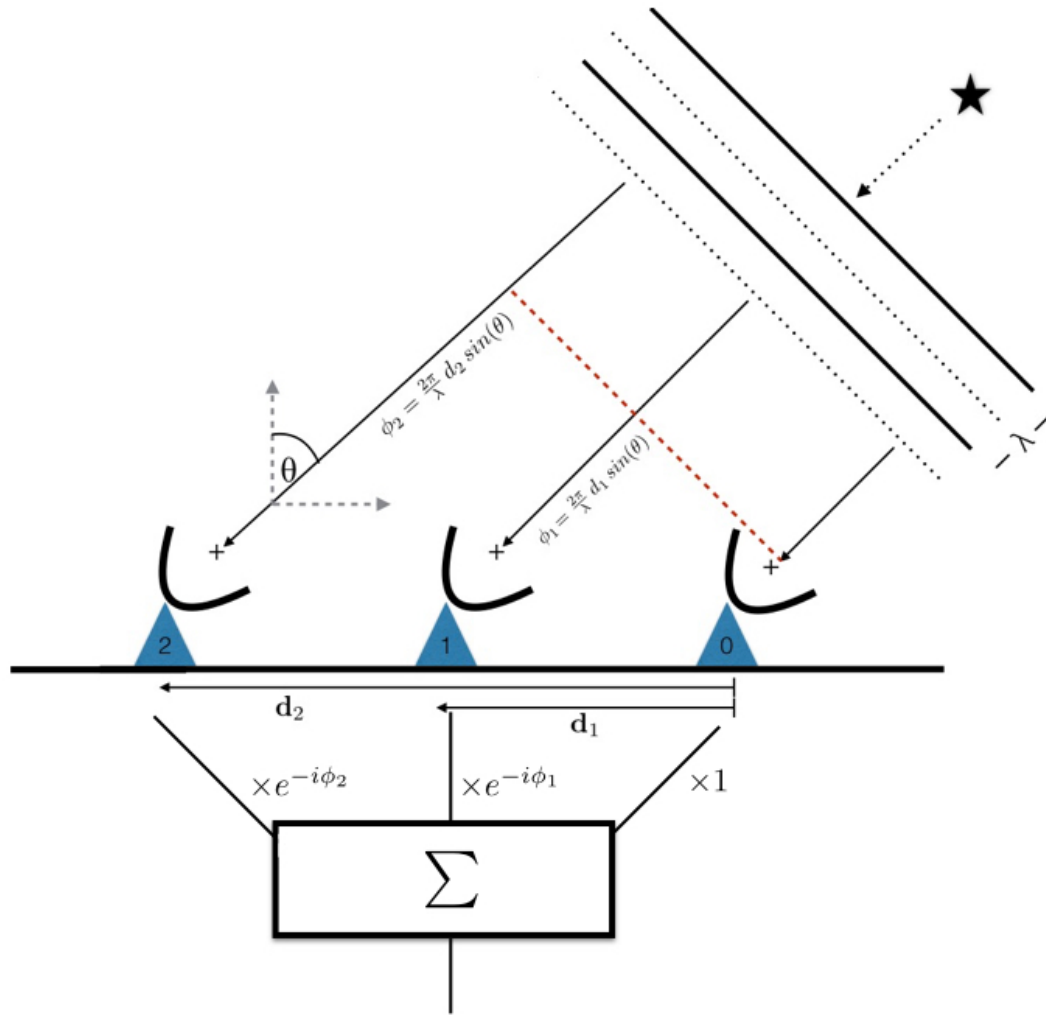


Figure 2.1: Diagrammatic example of a three-element beamformer. The wavefront from a far-field point-source arrives at each antenna at different times, but the delay is calculable given an array configuration and a direction to the object. Complex weights can be applied to each antenna’s voltage time-stream to account for the geometric delay, allowing for the signals to be summed coherently.

To calculate the projection $\mathbf{d}_n \cdot \hat{\mathbf{k}}$, we need to go from celestial coordinates, in this case equatorial, to geographic coordinates. This requires only a source location, an observer location, and an observing time. For the latter we use local sidereal time (LST), which is the *RA* of the local meridian. This can be determined by an observer’s longitude and a time, e.g. a Coordinated Universal Time (UTC). A source’s hour angle is simply the

Variable	Coordinate
δ	Source declination
RA	Source right ascension
LST	Local sidereal time
HA	Source hour angle
alt	Source altitude
az	Source azimuth
lat	Telescope latitude
lon	Telescope longitude

difference between LST and its RA ,

$$HA = LST - RA. \quad (2.7)$$

We use the standard interferometric (u, v, w) coordinate system to describe our baseline vector, \mathbf{d}_n . This is a right-handed coordinate system where u (east-west) and v (north-south) are in the plane whose normal is the zenith, and w measures the vertical direction (Thompson et al., 1986). They are defined in numbers of wavelengths, with $u = d_{ew}/\lambda$, $v = d_{ns}/\lambda$, and $w = d_{vert}/\lambda$. Eq. 2.6 can be expanded as,

$$\phi_n = 2\pi (u, v, w) \cdot \hat{\mathbf{k}} \quad (2.8)$$

$$= 2\pi \left(u \hat{\mathbf{u}} \cdot \hat{\mathbf{k}} + v \hat{\mathbf{v}} \cdot \hat{\mathbf{k}} + w \hat{\mathbf{w}} \cdot \hat{\mathbf{k}} \right), \quad (2.9)$$

where each projection component can be obtained using spherical trigonometry. Though we do not go through the derivation here, it is given by the following product,

$$\mathbf{d}_n \cdot \hat{\mathbf{k}} = \lambda \begin{pmatrix} u, & v, & w \end{pmatrix} \cdot \begin{pmatrix} -\cos\delta \sin HA \\ \cos(lat) \sin\delta - \sin(lat) \cos\delta \cos HA \\ \sin(lat) \sin\delta + \cos(lat) \cos\delta \cos HA \end{pmatrix}. \quad (2.10)$$

These phases are not only essential to beamforming but also for the fringestopping process, which is ubiquitous in interferometric analysis and is described in Sect. 2.4.1.

2.4 Pathfinder beamformer

2.4.1 Instrumental phases

In a real experiment, if the voltages from each antenna, x_n , are summed without any adjustment from those written in Eq 2.1, one should only expect noise and not a coherent beam. This is because we have assumed the wavefront's differential time-of-arrival across the array is the same time delay seen by the correlator. In fact each signal is further delayed by multiple steps in the signal chain, often randomly. Digital phases in the electronics can be added by the LNAs and FLAs; coaxial cables, whose lengths vary by up to a meter, can rotate the signal by multiple radians. Therefore in order to coherently sum across the array and beamform, the instrumental phases must be removed. If e_n is the true electric field on the sky as seen by each feed, then the thing we measure is the on-sky signal altered by an effective gain, g_n , and a noise term, n_n .

$$x_n = g_n e_n + n_n \quad (2.11)$$

We have lumped several terms into $g_n = |g_n|e^{i\phi_{g_n}}$, which is composed of a pointing-dependent beam term and any complex gain introduced once light hits the cylinder. Since we care primarily about the phase, we can decompose ϕ_{g_n} as,

$$\phi_{g_n} = \phi_{\text{beam}} + \phi_{\text{an}} + \phi_{\text{e}} + \phi_{\text{fpga}} \quad (2.12)$$

where ϕ_{beam} is the beam's phase for a given pointing, ϕ_{an} comes from the analog chain (dual-pol feed, coax, etc.), ϕ_{e} is any phase introduced in the electronics, and ϕ_{fpga} are phases applied in the F-engine.

Since the instrumental phases are effectively random, the simplest way to remove them is to solve for them empirically, usually from a point-source on the sky. The visibility definition from Eq. 1.2 on page 3 can be written in terms of the electric field on the sky

instead of brightness temperature. The correlation between antennas m and n will be given by the following integral,

$$V_{m,n} = \int d^2\hat{\mathbf{k}} g_m(\hat{\mathbf{k}}) g_n^*(\hat{\mathbf{k}}) e_m(\hat{\mathbf{k}}) e_n^*(\hat{\mathbf{k}}), \quad (2.13)$$

where $e_m(\hat{\mathbf{k}})$ is the complex electric field in the direction $\hat{\mathbf{k}}$ as seen by antenna m . We can evaluate this all-sky integral as if the sky's electric field were produced by a single point-source. This is tantamount to a delta function at a single direction on the sky.

$$V_{m,n}^{\text{ps}} = \int d^2\hat{\mathbf{k}} g_m(\hat{\mathbf{k}}) g_n^*(\hat{\mathbf{k}}) e_m(\hat{\mathbf{k}}) e_n^*(\hat{\mathbf{k}}) \delta(\hat{\mathbf{k}} - \hat{\mathbf{k}}_{\text{ps}}) \quad (2.14)$$

$$= g_m(\hat{\mathbf{k}}_{\text{ps}}) g_n^*(\hat{\mathbf{k}}_{\text{ps}}) e_m(\hat{\mathbf{k}}_{\text{ps}}) e_n^*(\hat{\mathbf{k}}_{\text{ps}}) \quad (2.15)$$

In these equations $\hat{\mathbf{k}}_{\text{ps}}$ is the only direction on the sky with a source in it — an approximation whose validity we will discuss below — and δ is a Kronecker delta function.

If we explicitly write the phase information of the sky's electric field and write its magnitude as a brightness temperature, we get,

$$V_{m,n}^{\text{ps}} = g_m(\hat{\mathbf{k}}_{\text{ps}}) g_n^*(\hat{\mathbf{k}}_{\text{ps}}) T(\hat{\mathbf{k}}_{\text{ps}}) e^{2\pi i \hat{\mathbf{k}}_{\text{ps}} \cdot \mathbf{d}_{mn}}. \quad (2.16)$$

Therefore a single correlation can be written as an intensity multiplied by a phase factor that is determined by the source direction's projection onto that correlation's baseline. Since that phase factor is calculable via Eq. 2.10, it can be removed in a process called “fringestopping”. The data can be inspected visually quite easily, since a transiting point-source will fringe as a function of time at a rate corresponding to the projected baseline length, but should not after fringestopping is applied. This is demonstrated with an inter-cylinder Cygnus A transit in Fig. 2.2.

The visibilities we measure can be thought of as the upper triangle of an $N \times N$

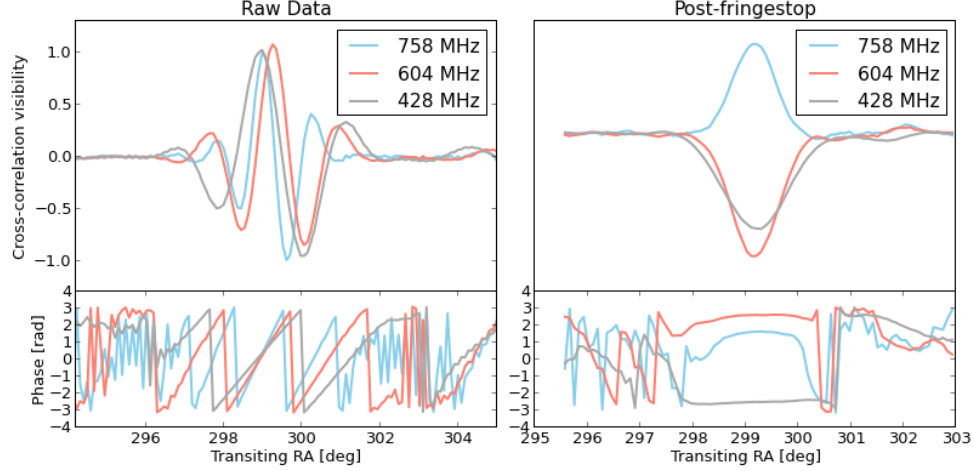


Figure 2.2: An example of the fringing process that is necessary for gain calibration off of a transiting point-source. Since the phase of a visibility will have a time- and frequency-dependent component, the measured correlation will fringe as the earth rotates in a chromatic way. This effect can be removed by multiplying each visibility by $e^{-i\phi_{m,n}(t,\nu)}$, as determined by Eq. 2.10. The top left panel shows the raw correlation between feeds 1 and 129 as a function of transiting RA , which are of the same polarization but on opposite cylinders, separated by 21 m. We plot three different frequencies. The left sub-figure shows the data before fringing, where the top panel is the complex visibility and the bottom panel is its corresponding phase. The slope, or fringe-rate, decreases at lower frequencies, as expected. The right panel show the same data after running it through the fringing pipeline. Though the resulting phases are near flat, implying that the baseline is no longer fringing, the visibilities are not purely real; this is because there are residual instrumental phases. These phases can be solved for using an eigendecomposition now that the array is phased up to a single point-source.

complex Hermitian matrix, \mathbf{V} . This is simply the outer product of the signal vector, \mathbf{x} , with its Hermitian conjugate.

$$\mathbf{V} = \mathbf{x}\mathbf{x}^\dagger \approx \begin{pmatrix} |g_0|^2 e_0^2 & \dots & & \\ & & g_n g_m^* e_n e_m^* & \\ & & \ddots & \\ & & & |g_N|^2 e_N^2 \end{pmatrix} \quad (2.17)$$

If the sky is composed of a single point-source then this matrix will be rank one, i.e. there is only one non-zero eigenvalue. One can see this by referring to Eq. 2.16 and noting that if the data has been fringestopped, then the phase component (which is different for each correlation) goes away. The sky temperature (which is the same for each correlation) can be factored out of Eq. 2.17, which then becomes:

$$\mathbf{V} = T(\hat{\mathbf{k}}_{\text{ps}}) \mathbf{g}\mathbf{g}^\dagger. \quad (2.18)$$

Therefore by diagonalizing the correlation matrix \mathbf{V} we get a complex eigenvector corresponding to the largest eigenvalue, and that eigenvector is proportional to the gain vector \mathbf{g} . The phase of this eigenvector will be an estimate for the instrumental phases, ϕ_{g_n} , up to some unknown global offset. The goodness of this calibration depends on the validity of our assumption that the correlation matrix is rank one. We can estimate the error on the calibration solution as the ratio of the second largest eigenvalue, λ_2 , to the largest, λ_1 . For typical frequencies we get values of $\frac{\lambda_2}{\lambda_1} \sim 2\%$ when using Cyg A or Cas A.

These algorithms have been implemented in a pre-beamforming pipeline written in **Python**. Every day a point-source transit is fringestopped and a calibration solution is solved for at each frequency. The source chosen depends on the solar time of its transit:

Since the sun is extraordinarily bright in our band it will be in our side-lobes as long as it is above the horizon, so the transit has to be at night for good calibration solutions. Historically, we have used Cygnus A in the spring and summer, Cassiopeia A in the summer and fall, and Tau A in the winter. Whatever we calibrate off of, the phases of that solution are written to pickle files that are then fed to the Pathfinder's FPGAs. The FPGA then applies complex gains after channelization, which in theory should provide the beamforming kernel with voltages whose phases are purely geometric.

2.4.2 First coherent light

Although the majority of the back-end was written within a couple of months, the beamformer required substantial on-sky testing and subsequent debugging. One important debugging tool came from utilizing the equivalence of the summed-and-squared high-cadence data that was produced by the beamformer with the full- N^2 integrated data. This is true because the correlation step does not erase any fundamental information about the electric field. The latter is nominally taken with ~ 21 second time samples for 32,896 correlation products coming from 256 feeds. The former is a sum over the feeds which can be integrated in time arbitrarily after squaring. Ignoring the time rebinning for a moment, we can write the squared formed beam as,

$$X_{\text{BF}} X_{\text{BF}}^* = (w_1 x_1 + w_2 x_2 + \dots + w_N x_N)(w_1 x_1 + w_2 x_2 + \dots + w_N x_N)^* \quad (2.19)$$

$$= |w_1|^2 |x_1|^2 + \dots + |w_N|^2 |x_N|^2 + \dots + w_1 w_2^* x_1 x_2^* + w_2 w_1^* x_2 x_1^* + \dots, \quad (2.20)$$

where, as before, w_n are the complex weights applied in the beamformer and x_n is a voltage stream from antenna n . This can be rewritten as the sum of the auto correlations and twice the real part of the recorded phase-shifted cross-correlations.

$$X_{\text{BF}} X_{\text{BF}}^* = \sum_{n \leq N} |w_n|^2 V_{n,n} + 2 \sum_{\substack{n,m \leq N \\ n < m}} \Re\{W_{n,m} V_{n,m}\} \quad (2.21)$$

In this equation we have let $W_{n,m} \equiv w_n w_m^*$. Since the correlation matrix is Hermitian, its top and bottom triangles are redundant and one needs only to record $\frac{1}{2}N(N+1)$ of the N^2 pairwise products. If we wrote all pairwise correlations, we would simply need to sum the correlation matrix after applying the relevant weights, i.e. summing after the Hadamard product, $\mathbf{W} \circ \mathbf{V}$. This is identical to Eq. 2.21 if both matrices \mathbf{W} and \mathbf{V} are Hermitian.

Using the equivalence we have just described, one can compare the output of the beamformer to the N^2 visibilities after applying complex weights and summing the correlations. This is effectively off-line beamforming, though the cadence is too slow for the science goals of the real beamforming back-end. As a first test, we would form a stationary beam with only two feeds and let a bright point-source like Cas A drift through, producing a fringe pattern. We would then take the corresponding Cas A transit from the correlated “cosmology” acquisition, using Eq. 2.21 and giving only non-zero weights to the two relevant feeds, and check if the two fringe patterns were identical.

We carried out a series of tests of escalating complexity. This included using more feeds in the sum, updating phases in real-time in order to track sources during a transit, and deliberately switching the weights with their conjugate to see if the fringe direction changed. Through these tests several bugs were discovered, such as spherical trigonometry errors in the phase calculations and a disagreement between one piece of code’s definition of LST .

The final hurdle was more fundamental to CHIME’s architecture, though in principle it should not affect the cosmology experiment. It was found through early pulsar observations that the beamformer was only summing coherently when the instrumental phases

that are removed in the FPGAs are solved for with the lower-triangle of the correlation matrix. In other words, instrumental phases were not properly removed in the correlator unless they were applied as $e^{+i\phi_{gn}}$ instead of $e^{-i\phi_{gn}}$, as one would expect. The perplexing thing was that in two years of analyzing the visibilities output by the correlator, nobody noticed anything surprising in the sign-convention. And indeed, when we started to look at the phase of the raw visibilities, we found the argument of an east-west baseline increases with time, which is what one expects from an upper-triangle correlator. This apparent paradox was solved by discovering *two* sign reversals, one in the F-engine and one in the X-engine, that effectively cancel each other out, but only if both are applied.

Our digitizers sample at 800 MHz, taking advantage of the observing band between 400-800 MHz being in the second Nyquist zone. However, when we channelize the incoming time-stream data in the FPGAs, the complex conjugation associated with the aliased second Nyquist zone was not considered during the Fourier transform. Therefore the channelized voltages leave the F-engine with an opposite sign in the exponential. When they are correlated in the X-engine it is also done in reverse order as,

$$V_{n,m} = x_n^* x_m, \quad (2.22)$$

as opposed to the upper-triangle correlation described by Klages et al. (2015),

$$V_{n,m} = x_n x_m^*. \quad (2.23)$$

The second sign convention error does not affect the beamformed output, since that data stream is never correlated. We therefore needed to account for this for the back-end to work. An example of an early verification of the beamformer's sign convention and the first successful tracking observation is shown in Fig. 2.3. The collaboration has decided to keep these sign conventions as is and make note of it going forward, rather than re-write any low-level software.

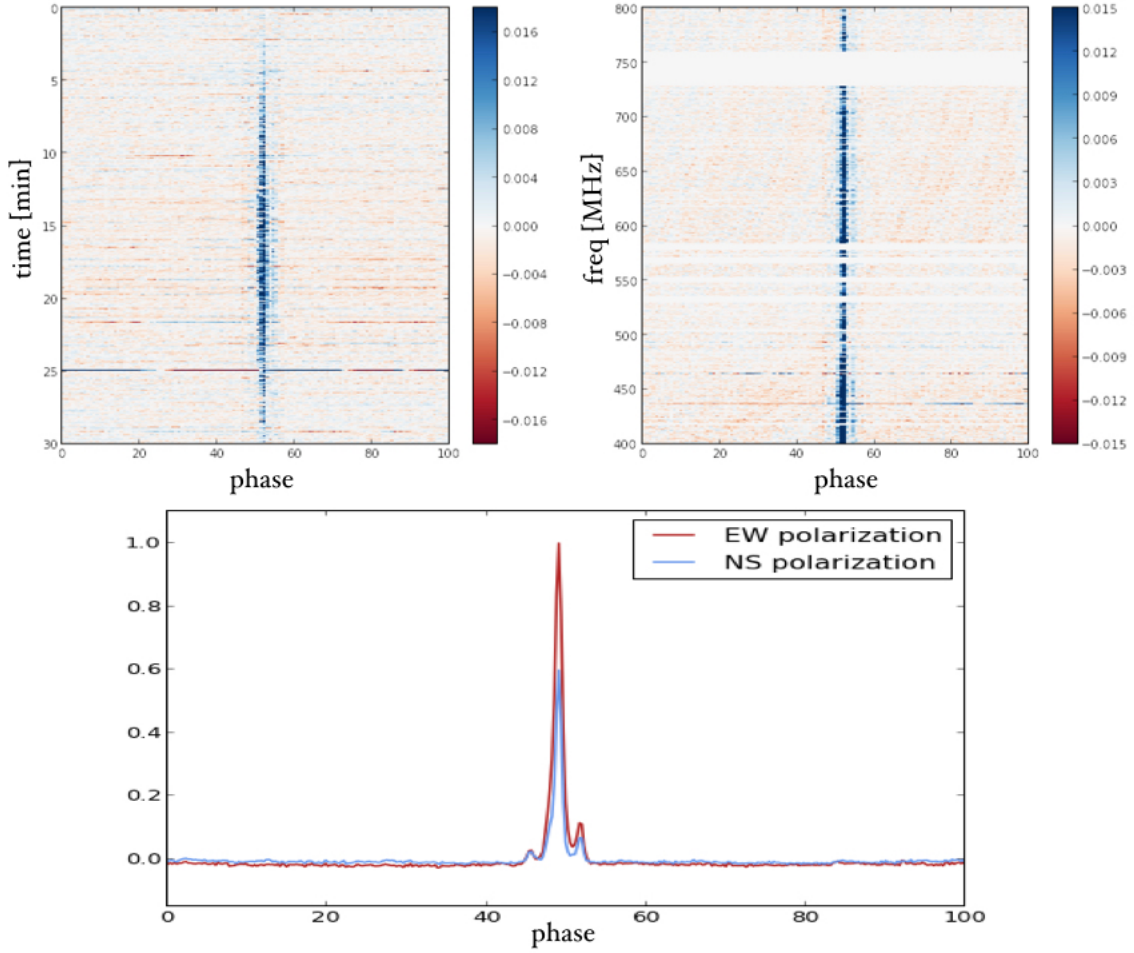


Figure 2.3: First coherent pulsar observations with CHIME. This brief observation of B0329+54 provided us with an idea of the instrument’s sensitivity and polarization response. Perhaps more significantly, it taught us that that our X-engine is a lower-triangle correlator, rather than upper-triangle like we thought, and that our F-engine *also* conjugates with the opposite sign. *top left*: waterfall plot of the pulsar’s Stokes I profile over the ~ 30 minutes when the source enters then exits our beam. *top right*: frequency vs. phase Stokes I, integrated over roughly 15 minutes. *bottom*: time- and frequency-averaged pulse profile for the two polarizations’ autocorrelations. The difference between the east-west and north-south beams give an estimate for Stokes Q, which includes both intrinsic polarization ($\sim 10\%$ for this source) and instrumental leakage.

2.5 FRB VLBI search

In 1967 Canada achieved an historic feat by doing the first ever successful very long baseline interferometry (VLBI) observation. The fringes were obtained between DRAO and ARO, with a baseline of 3,074 km (Broten et al., 1967). This result was given a “Milestone” award from The Institute of Electrical and Electronics Engineers (IEEE), which was also awarded for the inception of the Internet, transmission of transatlantic radio signals, and the discovery of Maxwell’s equations¹. We have attempted to recreate the same VLBI baseline, but instead of using the considerable spatial resolution on quasars as in 1967, we are attempting to localize FRBs, and in place of the 26 m telescope we will use the Pathfinder’s formed beam.

2.5.1 Motivation

The CHIME Pathfinder is meant to have only one synthetic beam. Its purpose is primarily to act as a test-bed for the more powerful pulsar and FRB back-ends that will be attached to the full four-cylinder CHIME. However since the Pathfinder is on sky at all times and the beamformer we have built does not interrupt the ongoing cosmology acquisition, we decided to build a preliminary FRB search. We also have as many as three other telescopes onto which we can mount CHIME feeds and observe in our band: the Algonquin Radio Observatory (ARO), the John A. Galt 26 m, and the Green Bank 140ft telescope. This would allow for the first ever VLBI detection of an FRB.

This is interesting for a few reasons. From a development standpoint it allows us to understand better various stages of the CHIME-FRB pipeline, including the rate of RFI false-positives, our algorithm’s search efficiency, and specs on the regularity and precision of instrumental gain removal. It will also give us a good sense of how the real CHIME beams behave on the sky.

Beyond just instrumental development, this work opens up several avenues for new

¹http://ethw.org/Milestones:List_of_IEEE_Milestones

science. Most interestingly, we could reasonably expect to see a few bursts per year in VLBI. Localization is by far the most important next step in determining the origin of FRBs, and such a long-baseline detection would achieve this. This particular VLBI array, whose baselines are thousands of kilometers, would provide the necessary spatial resolution to locate the source within its galaxy. This is demonstrated in Fig. 2.4. On top of this, we would not only detect a burst with milli-arcsecond resolution, but it would also be the first source in our band, at 400-800 MHz. We would be writing baseband and therefore we would have access to full-polarization information, which has only been true of two published FRBs.

The Pathfinder beam could be used on its own to constrain the location of FRBs via their brightness distribution. Specifically, we could test the claims made by Vedantham et al. (2016) who suggest there is now evidence for a flat fluence distribution of FRBs, implying that they are cosmological in nature (see Chapter ?? for our detailed statistical analysis of this issue). This would mean there are a relatively large number of ultra-bright bursts, and that survey speed is determined by FoV rather than thermal sensitivity. The Pathfinder would be an excellent tool to test this hypothesis, as a non-detection after multiple months would call it into question.

Finally, millisecond intensities could be written to disk and stored at little cost to the search. We could look for slow pulsars and rotating radio transients (RRATs), since the Galaxy is in our beam for a significant fraction of the day.

2.5.2 Implementation

We have had a working beamforming back-end on the CHIME Pathfinder since October 2015. In it, a beamforming kernel in the GPUs sends data over two 10 GBe lines to an acquisition node, `moose`, in the VLBI Data Interchange Format (VDIF) specification². Our version of VDIF has 5032-byte packets whose first 32 bytes contain header information,

²http://www.vlbi.org/vdif/docs/VDIF_specification_Release.1.1.1.pdf

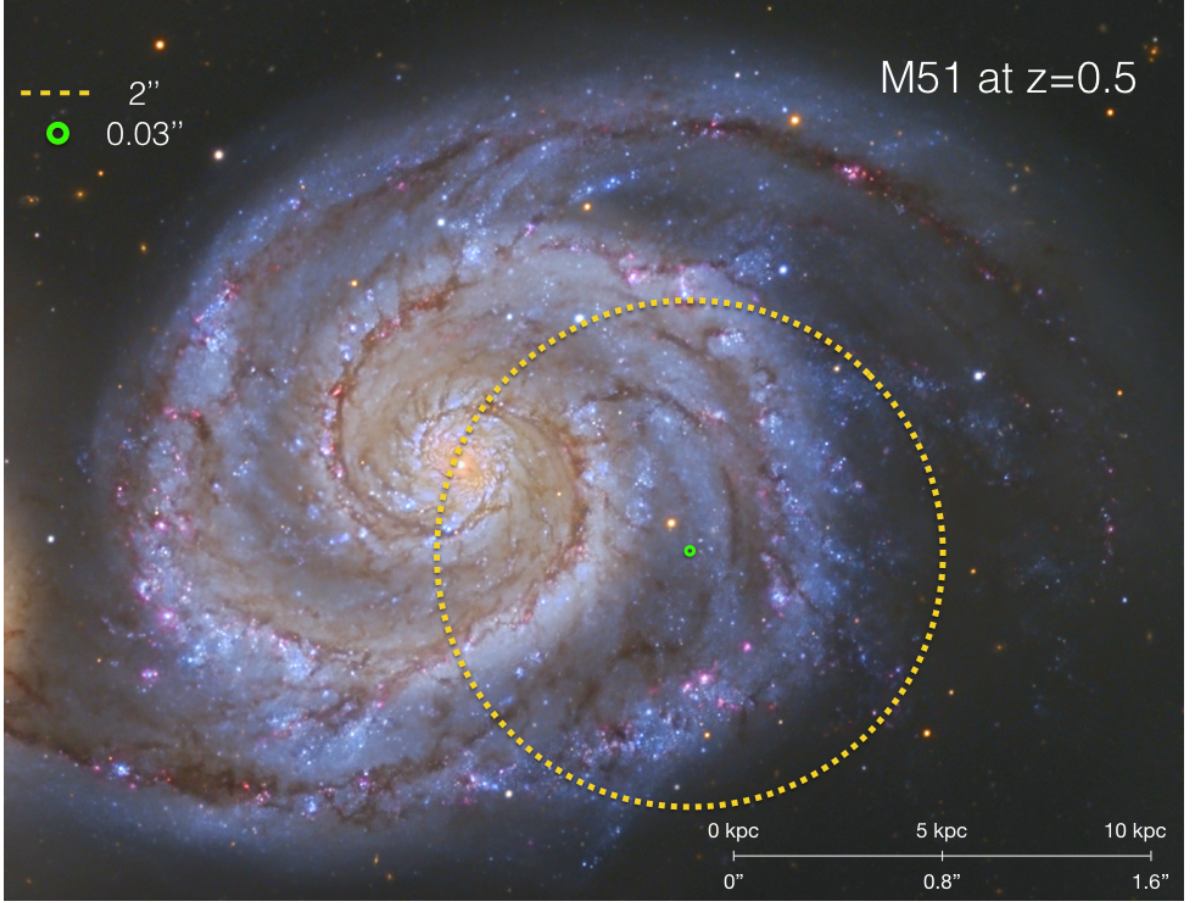


Figure 2.4: A visual demonstration of the difference between 30 milli-arcsecond resolution and an \sim arcsecond beam. This shows the need for extremely long baselines in a FRB VLBI effort. The image shows M51, which is about 20 kpc across, if it were at redshift 0.5. $2''$ resolution ($\sim 10^5$ wavelengths, or a ~ 50 km baseline at 600 MHz.) cannot distinguish between the Galactic center and the edge of the disk. On the other hand, $0.03''$ ($\sim 10^7$ wavelengths) can localize the source well within the Galaxy even at high redshifts. This is the resolution of the 3,074 km DRAO-ARO baseline in our band.

including labels for the polarization and frequency subset in that packet. The back-end has been used primarily for short tracking pulsar observations, but had stability issues on timescales of \sim days, meaning we could not run it for long periods without interfering with the regular cosmology acquisition. However in the past several months a number of new features were added that allow not only long-term beamforming captures, but also transient searching.

A real-time, multithreaded acquisition code that takes in the VDIF packets coming

out of the X-engine, and rearranges them to either be written to disk or search for FRBs³. Attached to this packet reader was a tree-dedispersion search code, some of which had been used before on Green Bank 100 m data and a real-time ARO search⁴. The CHIME acquisition software `kotekan` was altered in a number of ways, fixing the long-term stability issues in the beamforming kernel. These systems were synthesized into a real-time transient search back-end that has been on sky since May 2016. It is outlined in Fig. 2.5.2 on page 38.

Since CHIME is a transit telescope with a long north-south beam, our formed beam is effectively confined to the meridian. This means we must choose an optimal declination on which to park the beam. As a sanity check, we have spent roughly half the time pointed at the declination of pulsar B0329+54, which is the brightest switching source in the northern sky in our band. It is dispersed with $26.833 \text{ pc cm}^{-3}$ and its individual pulses are bright enough to detect, meaning our tree-dedispersion algorithm ought to find its individual pulses every time it transits. The search algorithm looks at time blocks of 100 seconds, searches for DMs between $10\text{--}2000 \text{ pc cm}^{-3}$ with widths between $1\text{--}100 \text{ ms}$, and nominally looks for peaks above 8σ . If it finds something it “triggers” and writes out an image file containing the peak in DM / arrival time space, a dedispersed waterfall plot, a dedispersed pulse profile, and a fluence frequency spectrum. An example of the B0329+54 trigger output is shown in Fig. 2.6. It also writes `numpy` arrays containing the squared and summed intensity data. It then moves on to the next block of 100 seconds, overlapping with the previous one by 18 seconds, and repeats those steps.

2.5.3 ARO FRB search

The ARO’s 46 m antenna has been mounted with a 400–800 MHz CHIME clover-feed that was specially built to account for the reflector’s focal ratio. We have implemented a similar back-end to the one operating at DRAO. Luckily, the computing requirements

³https://github.com/kmsmith137/ch_vdif_assembler

⁴https://github.com/kiyo-masui/burst_search

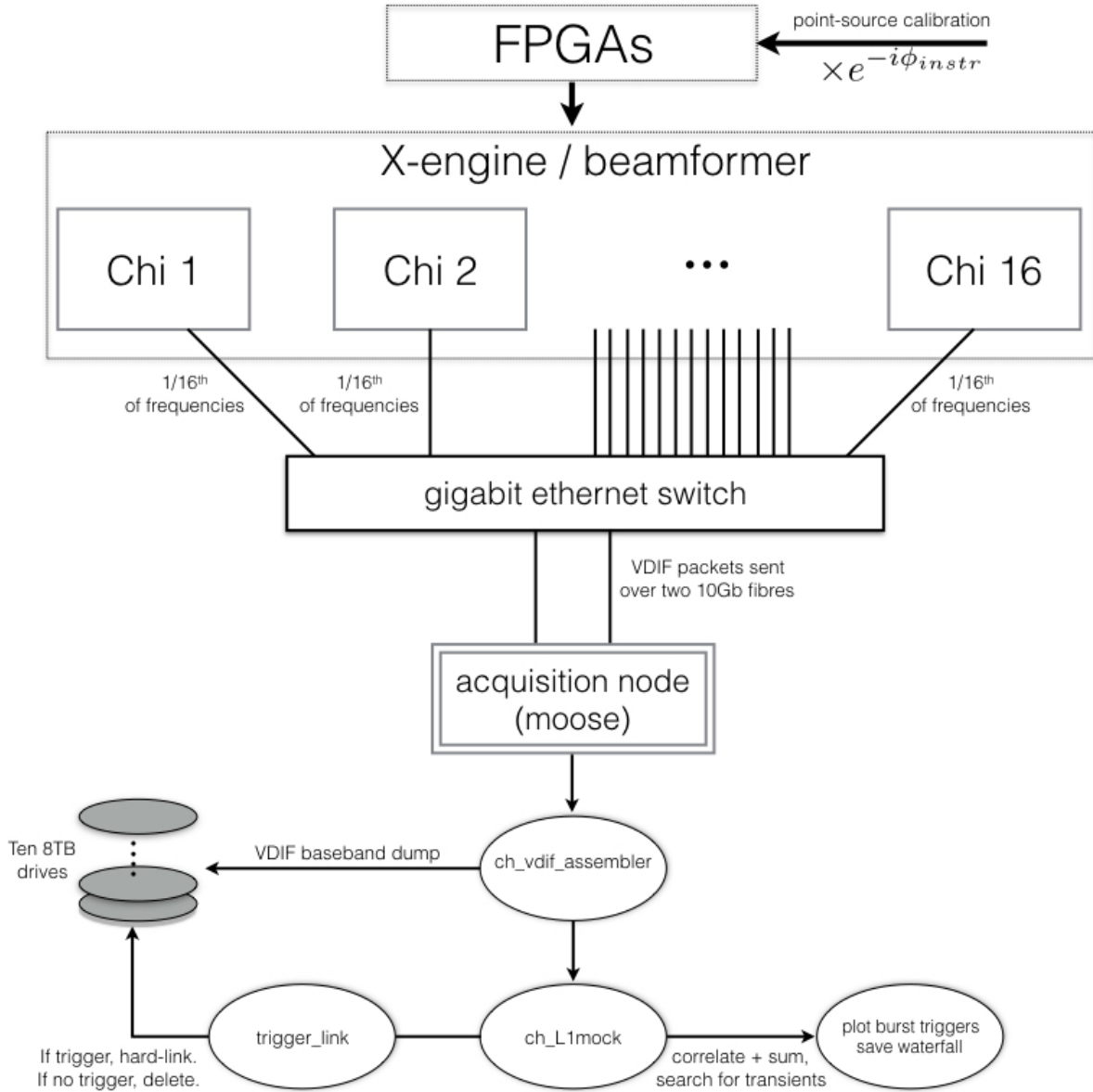


Figure 2.5: Block diagram of the beamforming back-end on CHIME Pathfinder. A calibration solution is obtained from a bright point-source transit, the phases of which are fed into the FPGAs where they are applied as a digital gain. All antenna signals are then sent to the X-engine, comprised of 16 GPU nodes. Each node received 64 frequency channels, applies geometric phases, then sums the voltage stream across all antennas with the same polarization. The two resultant beams are then sent to our acquisition machine **moose** as VDIF packets, where a multi-threaded capture code, **ch_vdif_assembler**, receives them. At this point the baseband data are either written to disk as scrambled baseband VDIF, or they are reorganized into contiguous time, polarization, frequency voltage arrays. The ordered data are searched for FRBs using a tree-dedispersion algorithm after squaring and integrating to \sim millisecond cadence. If there is a trigger, then the corresponding baseband data is hard-linked. Old files that haven't been hard-linked are deleted periodically.

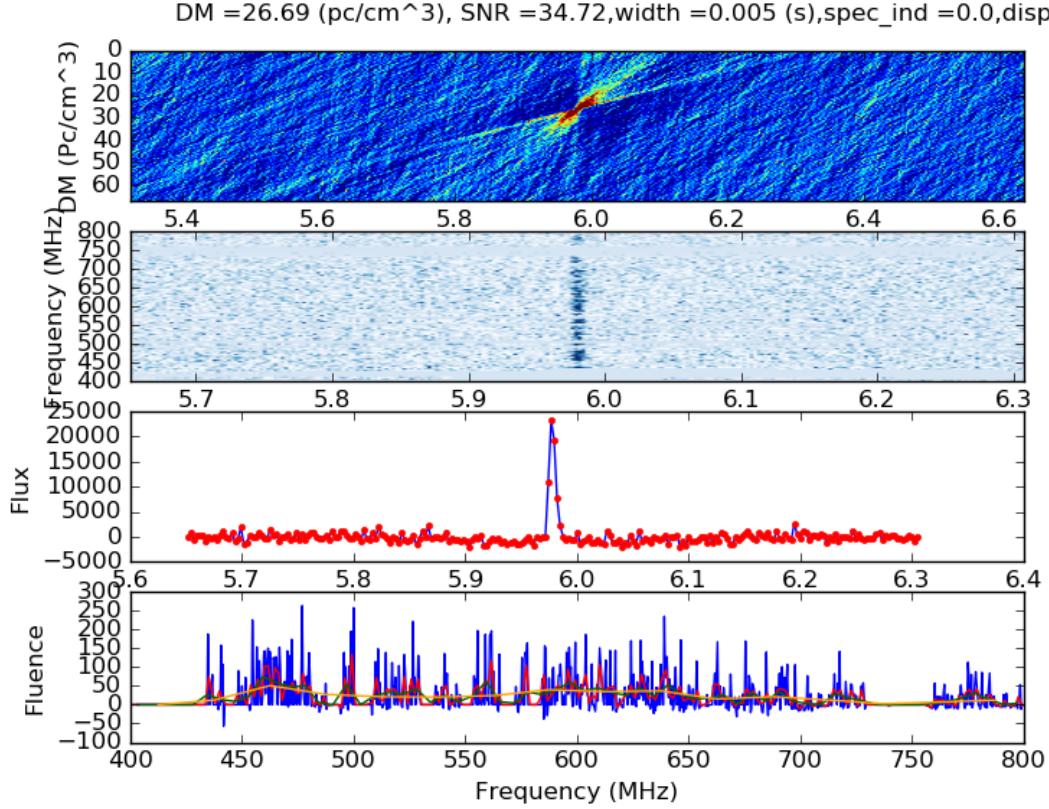


Figure 2.6: Example of a figure created after a trigger on the Pathfinder FRB search. This trigger was during the transit of pulsar B0329+54, on whose declination our synthetic beam was parked. Further information about the pulse is included at the top of the figure, including signal-to-noise ratio, width, and dispersion index. Though the beam is not well calibrated in absolute flux, this pulsar is of order 10 Jy, so this pulse might be half as bright as the original Lorimer burst (Lorimer et al., 2007). *Top panel:* The search results in dispersion measure vs. arrival time space. The red, butterfly-like cluster of points around DM of 25 pc cm⁻³ and arrival time 6 seconds into the 100 second block, shows the detection of a single B0329+54 pulse. *Second panel:* A frequency vs. time colour map showing the dedispersed pulse. *Third panel:* Pulse profile for this trigger, averaged over frequency after masking RFI and weighting by inverse system temperature. *Bottom panel:* Fluence vs. frequency plot of the pulse.

are less demanding. Since there is only one dual-polarization feed mounted on the dish, we need only one FGPA board and one processing node. At DRAO 1/16th of frequencies are handled by each GPU node, which means they arrive scrambled at the acquisition machine, *moose* (see Fig. 2.5.2). Software had to be written to re-order in time and frequency data in real-time. At ARO all 1024 frequencies arrive in contiguous blocks at

each frame, meaning we simply listen to a socket for the packets, square and sum, then run the transient search. The ARO back-end is outlined in Fig. 2.7.

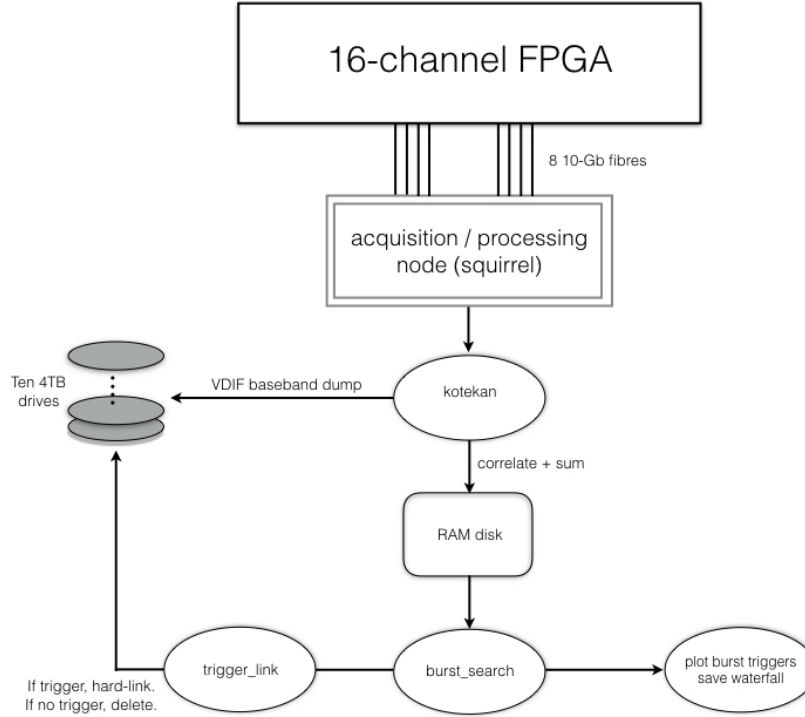


Figure 2.7: A block diagram of the basic FRB search set-up at ARO. A single 16-channel FPGA channelizes the 800 MSps data and sends 1024 frequencies to an acquisition node, **squirrel**, at a cadence of $2.56 \mu\text{s}$. Those data are squared, summed, and dumped to a RAM disk, where it is searched for FRBs between $10\text{-}2000 \text{ pc cm}^{-3}$.

2.5.4 Results

False positives

Most transient searches are plagued by non-celestial sources masquerading as astronomical events. In the case of DM searches on radio telescopes, these can be caused by RFI, numerical relics in the signal chain, or statistical fluctuations. At UTMOST, Caleb

et al. (2016) found 10^2 events per hour in transit mode across all beams. Petroff et al. (2015d) found the source of an elusive but persistent set of triggers to be due to an on-site microwave oven’s magnetron shutdown phase. These “Perytons” are unique in their conspiratorial ability to look like a real burst, but they are a subset of a broader zoo of RFI-induced false triggers.

At DRAO, although the region is officially protected from radio contamination, about 15% of the CHIME band is presently lost to RFI (see the bottom left panel of Fig. 2.8). Recently, Rogers Communications paid several billion Canadian dollars for a 700 MHz Long-Term Evolution (LTE) band for cellphone service. Unlike the satellite television stations that we see at 500-600 MHz, the LTE band fluctuates on timescales of milliseconds to seconds, which can affect a millisecond transient search. Fig. 2.8 shows an example of this RFI false positive from the LTE band.

To mitigate this, frequency channels that are known to be contaminated are masked out. Zeroing the LTE band, for instance, removed $\sim 90\%$ of the false-positive triggers. Once this was done, we find a false-trigger rate of approximately one per two hours. This is estimated by inspecting each trigger visually. Though the rate had been greatly reduced, it is still a 1000:1 ratio of false positives to real events in the case where we detect one FRB every three months (for a detailed estimate see Sect. ?? in Chapter ??). With this in mind, the SNR threshold was increased from 8σ to 9σ . This was done because the false triggers tend to occur with significance very close to the cutoff. Even if they are not perfectly Gaussian, the number of 6σ events is far larger than the number of 8σ events, of which there are many more than 10σ events.

This is less true for FRBs, whose brightness distribution are described by a power-law. Using a signal-to-noise cutoff of s_{\min} , the fraction of detected events one expects above s is given by,

$$f(> s) = \left(\frac{s}{s_{\min}} \right)^{-\alpha}. \quad (2.24)$$

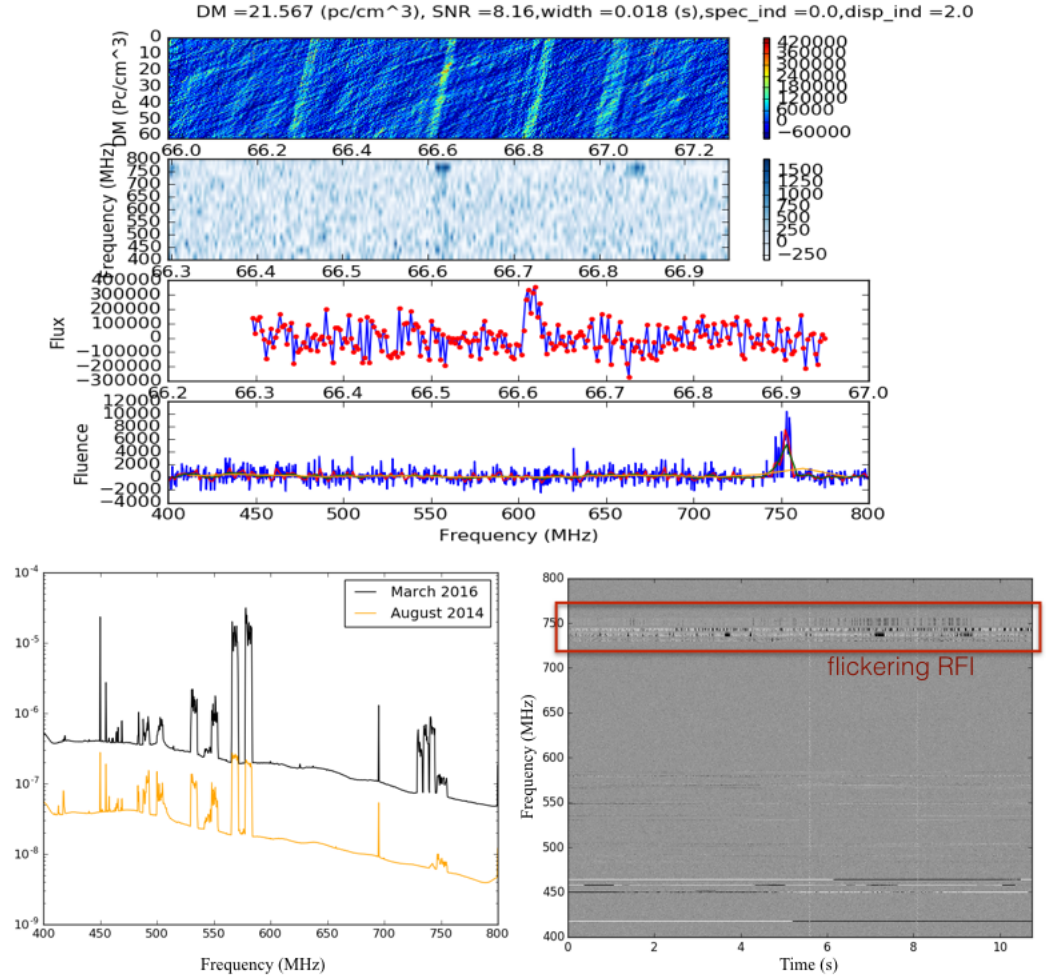


Figure 2.8: A false positive trigger caused by the flickering LTE band that, the likes of which caused $\sim 90\%$ of the alerts before it was removed. It is of course simple to reject; one can just mask out the relevant channels. However, it provides a useful example of the types of short-timescale RFI that can affect an FRB survey.

The signal-to-noise at which $f = 0.5$ is 12.7 and 19 for $\alpha = 1.5$ and $\alpha = 0.8$ respectively. The fraction of events one expects between $8-9\sigma$ is $f(> 8) - f(> 9) \approx 16\%$ for the Euclidean case, and 8% if α is 0.8. Therefore half the true events the experiment detects will unmistakably be celestial, whether they are cosmological or Euclidean, and by increasing the threshold to 9σ one only decreases the survey speed by of order ten percent.

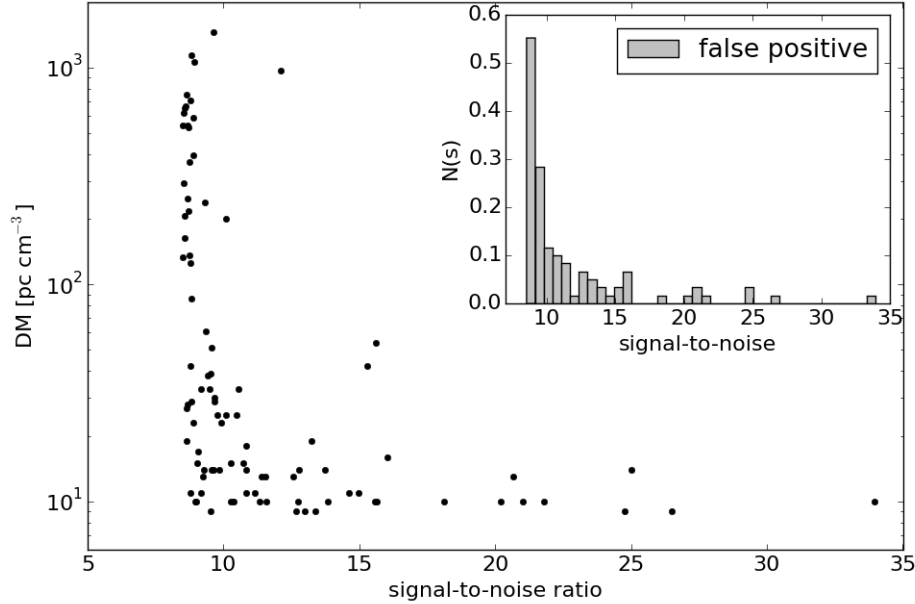


Figure 2.9: This figure shows the distribution of false-positives in DM and signal-to-noise. The embedded normalized histogram shows the clustering of events near the threshold of 8σ . One can see that by increasing the threshold to ~ 9 - 10 , half of all false triggers could be avoided. The scatter plot shows DM vs. signal-to-noise for the same set of triggers. The high-significance tail in the histogram seem to all be clustered at very low DMs, near the minimum DM that is searched (10 pc cm^{-3}). This makes it easy to differentiate truly “bright” events from high-signal-to-noise false positives.

A flat brightness distribution?

As we discuss in chapter ??, there is a large uncertainty in the FRB rate between 400-800 MHz. There is even greater uncertainty in the expected rate for a telescope like the CHIME Pathfinder. This is because at this time all FRBs have been detected with large collecting area, highly sensitive single-dish telescopes (GBT, Parkes, and Arecibo). Therefore in order to extrapolate the rate estimates on to the Pathfinder, which does not have much collecting area and whose beam is quite large, one needs to know the underlying brightness distribution. As we will show in Chapter ??, the rate depends on the product of the telescope’s field-of-view (FoV) and a thermal sensitivity term. For a single-feed receiver, the FoV is given by $\sim \left(\frac{\lambda}{D}\right)^2$, which scales inversely with collect-

ing area, A . The thermal component depends linearly on forward gain and therefore collecting area. Combining these, the rate is,

$$r_o = \text{FoV} \times (\text{sensitivity})^\alpha \quad (2.25)$$

$$\propto A^{-1} A^\alpha, \quad (2.26)$$

where α is the FRB flux distribution's power-law index, which is $3/2$ if FRBs are non-cosmological and Euclidean. If $\alpha < 1$, as is expected in the cosmological FRB scenario, then small telescopes are actually advantageous over large single-pixel telescopes since survey speed decreases with telescope size once $\alpha - 1$ is negative.

With a dish like the Pathfinder we expect the detection rate to be roughly 10 times higher if $\alpha \approx 0.8$ (cosmological scenario) compared to the Euclidean case. This is because its relatively low sensitivity per steradian requires there be large numbers of very bright bursts, which one gets from a flat distribution. Using non-detection in ~ 1.5 months of observing, we can estimate the values of α that are excluded by calculating the Poissonian probability of seeing zero given some expected value. As a simple model, assume the probability of seeing M FRBs given some expected number of events μ . Then,

$$P(M|\alpha, \mu) = \frac{\mu(\alpha)^M e^{-\mu(\alpha)}}{M!} \quad (2.27)$$

where μ can be calculated by extrapolating from other surveys in which FRBs have been seen. If we take the Pathfinder daily rate estimated in (Connor et al., 2016a) and presented in Chapter ?? and multiply it by the number of days on sky, we can calculate a p -value as a function of α . This is just given by $P(0|\alpha, \mu) = e^{-\mu}$ and is plotted in Fig. 2.10. We find that $\alpha < 0.61$ can be ruled out with 95% confidence. This is based on the Pathfinder sensitivity estimates we will use in Chapter ??, with $T_{\text{sys}} = 50$ K, 100 MHz of bandwidth (for reasons we will discuss), and a S/N threshold of 9σ . The dashed line on the right edge of the blue contour gives the probability of seeing zero FRBs in 45 days

of observing, assuming the 2σ upper-limit on the FRB rate in our band. The left edge uses the lower-bound on the rate, which is why seeing no events is quite likely, even when the spectrum is quite flat.

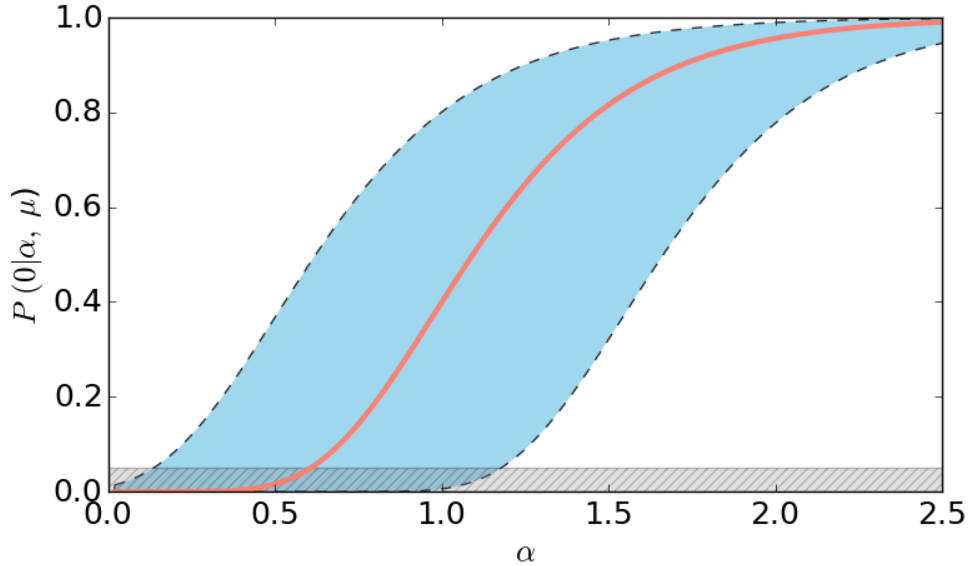


Figure 2.10: Early limits on the brightness distribution parameter α from the Pathfinder FRB search. The y -axis shows the Poissonian probability of seeing zero events assuming some α and an expected value based on the Pathfinder rate in (Connor et al., 2016a), with 45 days of observing. The rate, and therefore the expected number of detected bursts, is highly uncertain, which is why the blue region is so wide. The salmon curve shows the probability if we assume the central value of μ predicted by Connor et al. (2016a), and the dashed lines represent the 2σ bounds. The grey shaded region at the bottom of the figure shows the region that is ruled out with 95% confidence. Assuming the salmon curve, then $\alpha < 0.61$ is ruled out.

2.6 Conclusion

Digital beamforming is a powerful tool that affords modern radio telescopes enormous fields-of-view without sacrificing resolution. It is no longer strictly necessary to build large steerable reflectors, the cost of which scales roughly as diameter cubed⁵, since spatial filtering can be done in software. In this chapter we have walked through the basic

⁵https://www.astron.nl/mag/dokuwiki/lib/exe/fetch.php?media=radio_astronomy_lec.2_ma_garrett.pdf

mathematical formalism for beamforming. We have calculated the requisite geometric delays, which also allow us to “fringestop” the data. This process was put to use for phase-calibration of transiting point-sources, a step which is vital to beamforming.

The CHIME Pathfinder now has a stable beamforming back-end that runs in parallel with the full- N^2 cosmology acquisition. The back-end provides us with a tracking synthetic beam that dumps baseband data to disk with 1024 391 kHz channels at 2.56 microseconds. We have outlined the commissioning of this back-end, including the first coherent pulsar observations on CHIME.

We have also described a new project to localize FRBs with milli-arcsecond resolution using VLBI between Penticton, BC and Algonquin Park, Ontario. The first component of this project is a real-time transient search on the Pathfinder’s formed beam, which has been on-sky searching since early May 2016. Though we have not found any FRBs yet, the non-detection allows us to test the cosmological-origin hypothesis. This is because FRBs coming from $z \approx 0.3 - 1$ will have a flatter flux distribution than a more local population, which will obey $N(> S) \propto S^{-1.5}$. The cosmological hypothesis implies that there exists surplus of ultra-bright bursts that could be seen by a relatively insensitive instrument like that Pathfinder. We found that with 45 days on-sky and using conservative estimates for the telescope’s sensitivity, we can rule out $\alpha < 0.61$ with 95% confidence.

The ARO FRB search, which will complete the 3×10^3 km baseline, was described. It has a similar set-up to the system at DRAO, except with reduced computational complexity: each packet contains all 1024 contiguous packets. Once ARO is running its search, the S/N threshold there and on the CHIME Pathfinder search will be decreased to allow for coincident detection. If both locations trigger with the same DM at the same time, baseband voltage data will be written to disk and the telescopes will be correlated against each other. This could allow for several sub-milli-arcsecond FRB detections per year.

Bibliography

Bagchi, M., Nieves, A. C., & McLaughlin, M. 2012, MNRAS, 425, 2501

Bandura, K. e. a. 2014, in Society of Photo-Optical Instrumentation Engineers (SPIE) Conference Series, Vol. 9145, Society of Photo-Optical Instrumentation Engineers (SPIE) Conference Series, 22

Barrau, A., Rovelli, C., & Vidotto, F. 2014, Phys. Rev. D, 90, 127503

Berger, P., Newburgh, L. B., Amiri, M., et al. 2016, ArXiv e-prints, arXiv:1607.01473

Broten, N. W., Locke, J. L., Legg, T. H., McLeish, C. W., & Richards, R. S. 1967, Nature, 215, 38

Burke-Spolaor, S., Bailes, M., Ekers, R., Macquart, J.-P., & Crawford, III, F. 2011, ApJ, 727, 18

Caleb, M., Flynn, C., Bailes, M., et al. 2016, MNRAS, 458, 718

Champion, D. J., Petroff, E., Kramer, M., et al. 2016, MNRAS, arXiv:1511.07746

Connor, L., Lin, H.-H., Masui, K., et al. 2016a, MNRAS, 460, 1054

Connor, L., Pen, U.-L., & Oppermann, N. 2016b, MNRAS, 458, L89

Connor, L., Sievers, J., & Pen, U.-L. 2016c, MNRAS, 458, L19

Cordes, J. M., & Wasserman, I. 2016, MNRAS, 457, 232

Danish Khan, M. 2014, ArXiv e-prints, arXiv:1404.5080

Dodin, I. Y., & Fisch, N. J. 2014, ApJ, 794, 98

Drake, S. 1978, Galileo at work : his scientific biography

Falcke, H., & Rezzolla, L. 2014, A&A, 562, A137

Faraday, M., & Martin, T. 1936, Faraday's Diary: Nov. 24, 1855-Mar. 12, 1862, Vol. 7
(G. Bell and sons, ltd.)

Goldreich, P., & Sridhar, S. 2006, ApJ, 640, L159

Hewish, A., Bell, S. J., Pilkington, J. D. H., Scott, P. F., & Collins, R. A. 1968, Nature,
217, 709

Jansky, K. G. 1933, Nature, 132, 66

Kashiyama, K., Ioka, K., & Mészáros, P. 2013, ApJ, 776, L39

Katz, J. I. 2014, ApJ, 788, 34

—. 2016, Modern Physics Letters A, 31, 1630013

Keane, E. F., Stappers, B. W., Kramer, M., & Lyne, A. G. 2012, MNRAS, 425, L71

Keane, E. F., Johnston, S., Bhandari, S., et al. 2016, Nature, 530, 453

Klages, P., Bandura, K., Denman, N., et al. 2015, ArXiv e-prints, arXiv:1503.06203

Loeb, A., Shvartzvald, Y., & Maoz, D. 2014, MNRAS, 439, L46

Lorimer, D. R., Bailes, M., McLaughlin, M. A., Narkevic, D. J., & Crawford, F. 2007,
Science, 318, 777

Lyne, A. G., & Graham-Smith, F. 1998, Pulsar astronomy

Lyutikov, M. 2002, *ApJ*, 580, L65

Lyutikov, M., Burzawa, L., & Popov, S. B. 2016, ArXiv e-prints, arXiv:1603.02891

Macovski, A. 1983, *Medical Imaging Systems*, Prentice-Hall information and system sciences series (Prentice-Hall)

Madau, P. 2000, ArXiv Astrophysics e-prints, astro-ph/0005106

Manchester, R. N., & Taylor, J. H. 1977, *Pulsars*

Maoz, D., Loeb, A., Shvartzvald, Y., et al. 2015, *MNRAS*, 454, 2183

Masui, K., Lin, H.-H., Sievers, J., et al. 2015, *Nature*, 528, 523

Newburgh, L. B., Addison, G. E., Amiri, M., et al. 2014, in *Proc. SPIE*, Vol. 9145, Ground-based and Airborne Telescopes V, 91454V

Oppermann, N., Connor, L., & Pen, U.-L. 2016, ArXiv e-prints, arXiv:1604.03909

Oppermann, N., Junklewitz, H., Greiner, M., et al. 2015, *A&A*, 575, A118

Parsons, A., PAPER, & Kilimetre Array South Africa, S. 2014, in *American Astronomical Society Meeting Abstracts*, Vol. 223, American Astronomical Society Meeting Abstracts #223, 404.04

Pen, U.-L., & Connor, L. 2015, *ApJ*, 807, 179

Pen, U.-L., & Levin, Y. 2014, *MNRAS*, 442, 3338

Perlmutter, S., Aldering, G., Goldhaber, G., et al. 1999, *ApJ*, 517, 565

Peterson, J. B., Bandura, K., & Pen, U. L. 2006, ArXiv Astrophysics e-prints, astro-ph/0606104

Petroff, E., Bailes, M., Barr, E. D., et al. 2015a, *MNRAS*, 447, 246

—. 2015b, MNRAS, 447, 246

Petroff, E., Johnston, S., Keane, E. F., et al. 2015c, MNRAS, 454, 457

Petroff, E., Keane, E. F., Barr, E. D., et al. 2015d, MNRAS, 451, 3933

Petroff, E., Barr, E. D., Jameson, A., et al. 2016, ArXiv e-prints, arXiv:1601.03547

Piro, A. L. 2016, ApJ, 824, L32

Popov, S. B., & Postnov, K. A. 2007, ArXiv e-prints, arXiv:0710.2006

Rickett, B. J. 1977, ARA&A, 15, 479

Riess, A. G., Filippenko, A. V., Challis, P., et al. 1998, AJ, 116, 1009

Scholz, P., Spitler, L. G., Hessels, J. W. T., et al. 2016, ArXiv e-prints, arXiv:1603.08880

Spitler, L. G., Scholz, P., Hessels, J. W. T., et al. 2016, Nature, 531, 202

Stinebring, D. R., McLaughlin, M. A., Cordes, J. M., et al. 2001, ApJ, 549, L97

Tegmark, M., & Zaldarriaga, M. 2009, Phys. Rev. D, 79, 083530

Thompson, A. R., Moran, J. M., & Swenson, G. W. 1986, Interferometry and synthesis
in radio astronomy

Thornton, D., Stappers, B., Bailes, M., et al. 2013, Science, 341, 53

Tingay, S. J., Goetze, R., Bowman, J. D., et al. 2013, PASA, 30, e007

Totani, T. 2013, PASJ, 65, L12

van Haarlem, M. P., Wise, M. W., Gunst, A. W., et al. 2013, A&A, 556, A2

van Leeuwen, J. 2014, in The Third Hot-wiring the Transient Universe Workshop, ed.
P. R. Wozniak, M. J. Graham, A. A. Mahabal, & R. Seaman, 79–79

van Veen, B. D., & Buckley, K. M. 1988, IEEE ASSP Magazine, 5, 4

Vedantham, H. K., Ravi, V., Hallinan, G., & Shannon, R. 2016, ArXiv e-prints, arXiv:1606.06795

Williams, P. K. G., & Berger, E. 2016, ApJ, 821, L22

Zrnic, D. S., Kimpel, J. F., Forsyth, D. E., et al. 2007, Bulletin of the American Meteorological Society, 88, 1753

Zwicky, F. 1933, Helvetica Physica Acta, 6, 110